ABSTRACT

Title of Dissertation: SYSTEM IDENTIFICATION AND DE-CONVOLUTION OF A CLASS OF MULTI-CHANNEL WAVE PROPAGATION SYSTEMS FOR UNOBTRUSIVE CARDIOVASCULAR HEALTH MONITORING

Zahra Ghasemi, 2019

Dissertation directed by: Associate Professor, Jin-Oh Hahn, Mechanical Engineering Department

The main goal of this thesis is to improve the cardiovascular health monitoring by developing a novel model-based blind system identification approach. This research lies on the core idea that the central aortic blood pressure (BP) waveform can be estimated from as few as two non-invasive circulatory signals.

To achieve this goal, first, we formulated a physiological model for the class of multi-channel systems with non-invasive BP measurements and expressed it as a blind system identification problem. We verified this model for estimating the central blood pressure waveform from pulse volume records (PVR) signals from arm and leg, collected from 10 human subjects. The results showed that the proposed approach could estimate central aortic blood pressure waveform accurately. The average root-mean-squared error associated with the central aortic blood pressure waveform was 4.1 mmHg while the average errors associated with central aortic systolic and pulse pressures were 2.4 mmHg and 2.0 mmHg respectively.

Afterward, we compared this method with a population-based technique to calculate cardiovascular risk predictors. First, we used the same approach to estimate the central blood pressure waveform from two non-invasive peripheral waveforms and then, calculated cardiovascular risk predictors. Experimental results obtained from 164 human subjects with a wide blood pressure range showed that this approach could estimate cardiovascular risk predictors accurately. Further analysis showed that the suggested approach outperformed a generalized transfer function regardless of the degree of pulse pressure amplification, but especially in high and low amplification ranges.

Finally, a new closed-loop approach to input de-convolution in coprime multi-channel systems based on state estimation techniques is proposed. This approach is based on the idea that the unknown input signal in a multi-channel system may be regarded as a state variable to be estimated from multiple output signals of the system. The validity and potential of the approach were illustrated using the clinically significant case study of estimating central aortic BP waveform from two non-invasively peripheral arterial pulse waveforms. The proposed algorithm could reduce the root-mean-squared error associated with the central aortic blood pressure by up to 27.5% and 28.8% relative to two conventional central aortic blood pressure estimation techniques: open-loop inverse filtering and peripheral arterial pulse waveforms scaled to central aortic diastolic and mean pressures.

SYSTEM IDENTIFICATION AND DE-CONVOLUTION OF A CLASS OF MULTI-CHANNEL WAVE PROPAGATION SYSTEMS FOR UNOBTRUSIVE CARDIOVASCULAR HEALTH MONITORING

By

Zahra Ghasemi

Dissertation submitted to the Faculty of the Graduate School of the
University of Maryland, College Park, in partial fulfillment
of the requirements for the degree of
Doctor of Philosophy
2019

Advisory Committee:
  Associate Professor Jin-Oh Hahn, Chair
  Professor Alison Flatau, Dean's Representative
  Professor Balakumar Balachandran
  Professor Amr Baz
  Associate Professor Nikhil Chopra

Dedication

To my beloved mother and father,

who always encourage me to success

To my beloved husband,

who always supports me

Acknowledgments

The completion of this work could not have been possible without assistance and support of so many people over these 4.5 years. I particularly would like to express my deep appreciation to the following:

First and foremost to Dr. Jin-Oh Hahn for all his support and guidance as my Ph.D. advisor. Without his support, I could not achieve so much success during my presence at UMD.

I also want to show my gratefulness to our collaborators at the University of Maryland Medical center especially Dr. Anuj Gupta, whose help was essential in completing the clinical study. I also truly appreciate our international collaborators from the National Yang-Ming University of Taiwan especially Dr. Hao-min Cheng who kindly provided us with a large dataset to verify our proposed approach.

I am grateful for the professional guidance and assistance from Professor Rajesh Rajamani and his Ph.D. student Woongsun Jeon from the University of Minnesota. Their insights assisted us in expanding our proposed de-convolution algorithm.

Also, I would like to thank Professors Balakumar Balachandran, Amr Baz, Nikhil Chopra, and Alison Flatau from UMD for serving on my dissertation committee. Their time and constructive feedback on this work improved the quality considerably.

And lastly, I would like to show my respect to my colleagues Dr. Chang-Sei Kim and Albert Lee for working closely as a team and my other greatest friends at our laboratory for control and information system, Alex Lo, Ali Tivay, Azin Mousavi, Bahram Parvinian, Mohammad Al Salti, Nima Fazeli, Peyman Yousefian, Ramin Bighamian,

Shiva Ebrahim Nejad, Stephani Ober, Yang Yao, Xin Jin, Junxi Zhu, and Dr. Sungtae Shin for all their support and friendship.

I gratefully acknowledge the funding sources that make this work possible. This research was funded by the National Institute of Science (NSF) under Grants IIS-1404436 and IIS-1403004.

Finally, I cannot be thankful enough from my mother and father; who always encourage me to seek success, my husband, Ali; who always support me, and my brother, Taha for all his wise advice. I also want to thank my greatest family members and friends whose emotional support empowered me through all these years.

Table of Contents

List of Tables

List of Figures

List of Abbreviations

ABP	Arterial Blood Pressure
BP	Blood Pressure
CV	Cardiovascular
CVD	Cardiovascular Disease
DBP	Diastolic Blood Pressure
GTF	Generalized Transfer Function
ITF	Individualized Transfer Function
LMI	Linear Matrix Inequality
MAP	Mean Arterial Pressure
MBSI	Multi-Channel Blind System Identification
PP	Pulse Pressure
PP	Pole Placement
PTT	Pulse Transit Time
PVR	Pulse Volume Recording
PWV	Pulse Wave Velocity
RMSE	Root-Mean-Squared Error
SBP	Systolic Blood Pressure
SLS	Standard Linear Solid
TL	Tube-Load Model
TLG	Tube-Load model augmented by a gain
TLS	Tube-Load model augmented by a SLS model
TLV	Tube-Load model augmented by a Voigt model
UIO	Unknown Input Observer

Chapter 1: Introduction

1.1. Background

1.1.1. Cardiovascular (CV) Health and Cardiovascular Diseases

Cardiovascular diseases (CVD) such as stroke, atherosclerosis, and heart failure are the leading cause of death in the US and around the world at current years. According to American Heart Association's statistics, it is estimated that 92.1 million American adults (1 out of every 3 adults) suffer from CVD, which is projected to increase to 45.1% of the US population by 2035. Also in 2016, 36.5% of all deaths around the world were caused by CVD, which has increased by 14.5% from 2006 to 2016. Although the rate of death caused by CVD decreased by 14.5% from 2006 to 2016, it is still responsible for one death every 40 seconds in the US [1].

From another point of view, the estimated direct and indirect cost of CVD was $351.2 billion in 2014-2015 in USA and is expected to rise to $749 billion by 2035. Comparing the direct cost of CVD which was $213.8 billion were so higher than the cancer which was $84 billion [1]. All these data indicate the importance of early detection and timely treatment of CVDs.

1.1.2. CV Risk Predictors

CV risk factors are the characteristics or attributes of the cardiovascular system that indicate the increased risk of developing CVDs. By analyzing the arterial Blood pressure (BP) waveform, different parameters can be extracted to predict CVD. Systolic blood pressure (SBP, the maximum arterial pressure during contraction of the left ventricle of the heart), Diastolic blood pressure (DBP, the minimum arterial pressure during dilatation of the ventricles of the heart) and pulse pressure (PP, The numeric difference between SBP and DBP) are some of the CVD risk predictors that have been shown to have direct correlation with CV events [2], [3].

In addition, central BP, pulse wave velocity (PWV) is considered as an important CV risk predictors. PWV is the velocity of BP waveform traveling through the arterial tree and indicates the arterial stiffness, especially for older populations [4]. When the arterials are stiffed (loss of elasticity) especially as age goes up, the pulse wave is propagated at an increased velocity. One acceptable way of calculating PWV is to measure the pulse transit time (PTT) non-invasively for a determined distance along the arterial tree. PTT is the propagation delay of the pulse BP waveform through the arterial tree. Since the distance can be determined, PWV can be calculated as well.

1.1.3. Techniques for Cardiovascular Health Monitoring

Due to wave propagation and reflection phenomena in artery tree, BP waveforms becomes progressively deformed as they propagate further away from the heart as shown in Figure 1-1. Therefore, central aortic BP, due to its proximity to the heart, has more clinical value than peripheral BP at distal locations. As a result, central BP is a significantly better predictor of CV events than brachial BP [5]–[9].

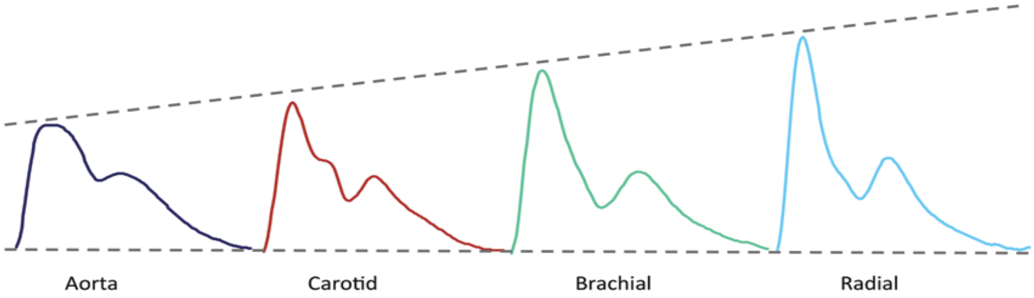

Figure 1-1- Blood pressure waveforms as moving from aorta to the radial artery [10]

Yet, central BP hasn't been widely used in clinical practices due to the risks and cost associated with its measurement [11]. For example, the measurement of central SBP and PP requires aortic catheterization [3], [12]–[15]; which is an invasive procedure and incurs clinical risk. An alternative non-invasive approach is carotid artery tonometry [16], [17]; but it involves costly probe and trained operators. The physics of this process is sensing the pressure within the artery by flattening a small part of the arterial wall under the probe. It is difficult to be certain of obtaining adequate applanation since the artery can move freely under the sensor and needs to be stabilized by pressure on other neck structures by the operator.

The measurement of aortic PP amplification and PWV (or equivalently, PTT), likewise, necessitates inconvenient carotid-femoral tonometry procedure [18]–[23]. On the other hand, peripheral BP (such as BP measured at arm and ankle) is, in general, easier to measure than central aortic BP. Measuring peripheral BP using cuff pulse volume records waveforms (PVR) is the most common and easiest method being employed in clinical practice these days. PVR is an arterial volume pulsation signal measured by the blood pressure cuff. When the BP cuff is placed at a distal site (e.g., arm and ankle) and inflated with constant, sub-diastolic pressure, PVR is measured as a small-amplitude oscillation in the pressure in the BP cuff invoked by the pulsatile nature of arterial BP. However, peripheral BP cannot serve as a direct surrogate of central aortic BP due to the well-known wave propagation and reflection phenomena explained before [24].

It is arguable that these cost and convenience issues have hampered early detection and timely treatment of CVD. Hence, novel technologies to complement the state-of-the-art CV health and risk predictor estimation techniques via convenient out-of-clinic monitoring and tracking of CV risk predictors may significantly improve the prevention, early detection, and treatment of CVD. However, there has been a substantial research effort to estimate central aortic BP from peripheral BP(s).

To overcome this challenge, research focuses on the methods to derive central aortic BP by the means of circulatory BP signals at distal body locations. Most of the methods are based on creating a population-based transfer function (between central aortic BP and peripheral BP) using BP signals measured from a group of subjects and using the averaged transfer function obtained from that group to the new individuals in order to predict the central BP waveform for new subjects. These methods known as generalized transfer function (GTF) methods, have greater clinical value over using peripheral BP signals but they still suffer from some limitations. Most importantly, the relationship between central and peripheral BP is not constant over the range of subjects and different physiologic conditions as it is assumed in these methods.

Another class of the methods is based on the individualized transfer function. In these methods known as individualized transfer function (ITF) methods, in order to estimate the central BP for each subject individually the identified transfer function for each person is used. So far this approach is developed to estimate central blood pressure of each subject via invasive peripheral BP waveforms [14].

1.2. Research Motivation

The ideal method for measuring CV risk is the one that is low-cost, easy to use, and non-invasive; also, the assessment must be personalized in order to achieve the best CV risk predictors. For the best practice, the central aortic waveform is needed, as discussed in the previous section the approaches in direct measuring central BP are either invasive (e.g. catheterization) or need trained operators (e.g. tonometry). Moreover, the current methods for estimating the central BP by means of measuring peripheral BPs are non-personalized (e.g. GTF methods) or need invasive peripheral BP measurements (e.g. invasive ITF methods). Therefore, all the existing methods lack from fulfilling some of these specifications.

One of the popular non-invasive methods in today's clinical practice is pulse volume recording (PVR). Due to its ease of measurement and morphological similarity to arterial BP (ABP) waveforms, PVR has been employed as a non-invasive surrogate of distal ABP waveform once it is calibrated with the SBP, MAP, and DBP values obtained by the BP cuff (e.g., oscillometry) [25]–[27]. However, PVR is not identical to ABP waveform in morphology. PVR originates from the volumetric pulsation in the arterial vessel created by the pulsatile ABP, which propagates to alter the pressure in the BP cuff via the tissues and cuff bladder. Hence, its waveform is influenced by the viscoelasticity associated with the artery (specifically, its pressure-volume relationship), surrounding tissues, and BP cuff inflated with compressed air, all at the site of measurement [26]. Therefore, it would be ideal if PVR waveforms that can be readily acquired in low-cost, out-of-hospital settings could be used with the tube-load model to deliver clinically useful cardiovascular health information.

1.3. Objective and Scientific Approach

Within the scope of this research, we seek to develop a low-cost and non-invasive method for personalized CV health assessment. As mentioned in section 1-2 current available methods suffer from fulfilling all the specifications needed. Our hypothesis is that CV health can be assessed by analyzing non-invasive circulatory signals acquired from routinely used low-cost medical sensors placed at body's peripheral locations (e.g. blood volume pulsations measured in standard blood pressure monitors). A unique strength of the proposed method is that it can derive an accurate estimation of personalized BP signal near the heart (rather than measuring it directly) via low-cost medical sensors, which enables non-invasive personalized assessment of CV health and risk parameters.

In the proposed method, the circulatory PVR signals measured at the body's peripheral locations are used to derive a personalized arterial tree model, which is then utilized to derive a personalized BP signal near the heart. Then, CV risk parameters are computed from the pair of estimated heart BP and measured peripheral circulatory signals.

To do so, a model-based algorithm is developed to compute (1) peripheral BP signal from non-invasive peripheral circulatory measurement, (2) personalized arterial tree model from peripheral BP signal(s), (3) a novel de-convolution algorithm to reconstruct the BP signal near the heart, and (4) personalized CV risk parameters based on the estimated BP signal near the heart. Then, the validity of the proposed method is studied using experimental data obtained from an international collaborator as well as our in-house data.

1.4. Dissertation Contribution

In this section, the main contribution of the proposed study is illustrated.

<u>Model-Based Blind System Identification Approach to Estimation of Central Aortic Blood Pressure Waveform from Non-Invasive Diametric Circulatory Signals:</u>

A model-based blind system identification approach is introduced to estimate the central aortic blood pressure waveform from non-invasive diametric circulatory signals. First, a mathematical model has been developed to reproduce the relationship between central aortic blood pressure waveform and a class of non-invasive circulatory signals at diametric locations by combining models to represent wave propagation in the artery, arterial pressure-volume relationship, and mechanics of the measurement instrument. Second, the problem of estimating central aortic blood pressure waveform from non-invasive diametric circulatory signals into a blind system identification problem is formulated. Third, the identifiability analysis is performed to show that the mathematical model could be identified, and its parameters determined up to an unknown scale. Finally, the feasibility of the approach is shown by applying it to estimate central aortic blood pressure waveform from two diametric pulse volume recording signals. Experimental results from 10 human subjects showed that the proposed approach could estimate central aortic blood pressure waveform accurately.

Estimation of CV Risk Predictors from Non-Invasively Measurements:

A novel multiple measurements information fusion approach is presented for the estimation of cardiovascular risk predictors from non-invasive pulse volume waveforms measured at the body's diametric locations. Leveraging the fact that diametric pulse volume waveforms originate from the common central pulse waveform, the approach estimates cardiovascular risk predictors in three steps by:

(1) Deriving lumped-parameter models of the central-diametric arterial lines from diametric pulse volume waveforms,

(2) Estimating central blood pressure waveform by analyzing the diametric pulse volume waveforms using the derived arterial line models, and

(3) Estimating cardiovascular risk predictors (including central SBP and PP, pulse pressure amplification, and PTT) from the arterial line models and central blood pressure waveform in conjunction with the diametric pulse volume waveforms.

Experimental results obtained from 164 human subjects with a wide blood pressure range showed that the approach could estimate cardiovascular risk predictors accurately. The approach may be integrated with already available dual-cuff devices to enable convenient out-of-clinic cardiovascular risk predictor monitoring in everyday life.

Observer-Based De-convolution Method:

A new closed-loop approach equipped with robustness against the channel dynamics inaccuracy is proposed. For this approach, we investigated the application of established state estimation to input de-convolution in coprime multi-channel systems. The central idea underlying this technique is to derive the unknown input signal in a coprime multi-channel dynamical system by regarding it as a state variable to be estimated from multiple output signals from the system.

Compared to the existing input de-convolution techniques whose integrity largely hinges upon the accuracy of the channel dynamics, the proposed approach may compensate for the adverse impact of the errors and uncertainties associated with the channel dynamics on input de-convolution by way of the state estimation technique’s corrective error feedback action.

The validity and potential of the approach were illustrated using the clinically significant case study of estimating central aortic BP waveform from two non-invasively acquired peripheral arterial pulse waveforms.

1.5. Dissertation Organization

The dissertation in arranged into the following chapters. In chapter 2, the existing work on estimating central arterial blood pressure, multi-channel blind system identification, as well as de-convolution filtering, are reviewed. In chapter 3 a model-based blind system identification approach to estimate the central aortic blood pressure waveform from non-invasive diametric circulatory signals is proposed. This model then is formulated and validated using experimental data from 10 human subjects. The new proposed de-convolution algorithm is introduced in chapter 4. The feasibility of this technique in improving the results is studied using experimental data as well. In chapter 5 a multiple measurement information fusion from non-invasively diametric pulse volume is introduced. This method is used to estimate cardiovascular risk predictors. This approach is also validated by the data set of 164 human subjects in that chapter. And finally, in chapter 6, the contribution of this dissertation and the direction for future work are summarized.

Literature Review

2.1. Estimating Central Arterial Blood Pressure

Chapter 2:

As mentioned earlier BP at aorta which we call it central BP, is a major CV risk predictors; however, Earlier techniques to estimate central aortic BP waveform from peripheral BP waveform involved a population-based mapping, based on the assumption that arterial properties are consistent and invariant in all subjects and at all times [11], [13], [16], [28], [29]. In a series of clinical investigations, such population-based techniques have been shown to yield a waveform that corresponds to central aortic BP waveform better than the peripheral BP waveform [13], [16]. However, arterial properties vary between subjects and also in each subject in response to changes in physiologic state. For this reason, population-based techniques are often prone to errors [30]–[33].

To overcome the weakness of population-based techniques and estimate central aortic BP waveform specific to individual subjects, blind system identification method (which is a class of system identification methods for systems with unknown inputs) has been employed in more recent work [13], [28], [31], [32], [41]–[44] . The idea in these techniques is that central aortic BP can be estimated from diametric BPs because the former is the common source to create the latter. To implement the techniques to estimate subject-specific central aortic BP waveform, theoretical foundations were developed to enable blind system identification of finite impulse response models [38]–[40], orthogonal basis function models [34] and physics-based wave propagation models [35]. These techniques showed promise when applied to invasive BP waveform data from animals and humans.

Among all suggested physical-based wave propagation models, the tube-load model has been validated to well reproduce the arterial wave propagation phenomena [41]. The model consists of a uniform lossless tube ended by a load $Z_L(s)$. The tube is characterized by its impedance Z_c, while $Z_L(s)$ is represented by a capacitance C_T and a resistance R_T (Figure 2-1). The capacitance represents the compliance of distal arteries and resistance is a representation of arterioles. In this model, the tube is a representative of a propagation path between the central aorta and peripheral artery and the load is the reflection site because of the arterial vessels [41].

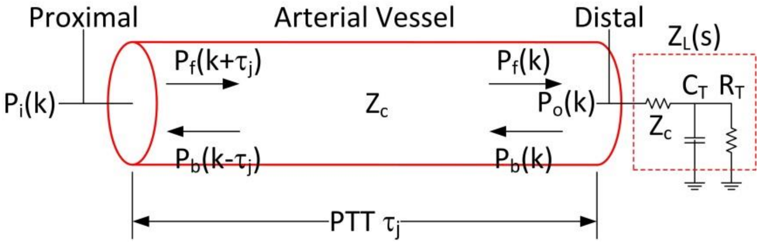

Figure 2-1- Tube-load model of arterial wave propagation. It is parameterized by pulse transit time τ and the lumped parameters η_1 and η_2 characterizing the wave reflection coefficient $\Gamma(s)$.

In sum, the model is parameterized by (i) the PTT associated with the tube τ and (ii) the parameters η_1 and η_2 characterizing the wave reflection coefficient $\Gamma(s)$. The discrete-time domain relation between proximal (P_i) and distal (P_o) BP waveforms are given by Eq. (2-1) where $\mathcal{Z}[\cdot]$ is the Z-transform.

$$\mathcal{Z}[P_i(t)] = \frac{1 + \Gamma_i(z)}{z^{\tau_i} + z^{-\tau_i}\Gamma_i(z)} \mathcal{Z}[P_0(t)] \tag{2-1}$$

Note that $\Gamma_i(z)$ can assume a variety of forms depending on the load model $Z_{Li}(z)$ used to represent the arterial bed beyond the distal site [41]:

$$\Gamma_i(z) = \frac{Z_{Li}(z) - Z_{ci}}{Z_{Li}(z) + Z_{ci}} \tag{2-2}$$

where Z_{ci} is the characteristic impedance associated with the distal site i.

2.2. Viscoelastic Models as Tissue Modeling [42]

Viscoelasticity is the combination of viscosity, which is a property of fluids, and elasticity, which is related to solids. Therefore, this behavior is for the materials that show both solid and fluid properties. The viscoelastic materials respond not only based on the amount of stress but also on how fast the stress is applied.

Different combinations of spring and dashpot are used as the empirical model for viscoelastic properties. Spring is representing the elastic behavior and dashpot is regard to viscosity. The Voight model, which is the parallel configuration of spring and dashpot, is the simplest model that is used for this type of materials. The performance of dashpot is restricted by the response of the spring, so this model is known as viscoelastic solid. This model is shown in figure 2-2.

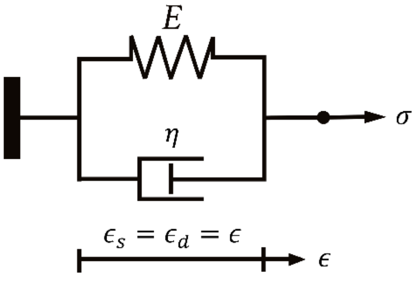

Figure 2-2- Voigt model [42]

Maxwell model consists of spring and dashpot in a series. Since dashpot can deform continually whereas the spring can deform up to a certain point, in this model the fluid aspect is more dominant than solid ones. That is why this model is known as viscoelastic fluid. This model is shown in figure 2-3.

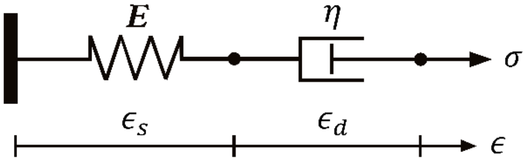

Figure 2-3- Maxwell model [42]

The Voigt and Maxwell are basic viscoelastic models that can be used to construct models that are more complex. One of the well-known models is Standard Linear Solid model (SLS) which is the combination of Voigt and spring in series as shown in Figure 2-4.

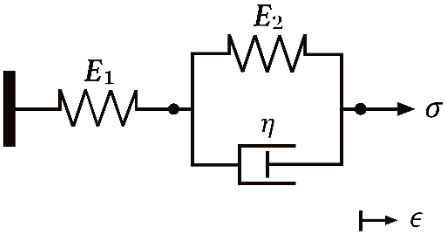

Figure 2-4- Standard Linear Solid model (SLS) [42]

All tissues can be considered as a composite material; their mechanical properties can be different in different direction and from a different location within the tissue and it will change over time by aging. Collagen and elastin fibers have the most affecting biomechanical behavior among different component of tissues. The elastin fibers mostly show elastic behavior while collagen fiber mostly show higher modulus viscoelastic behavior.

2.3. Multi-Channel Blind System Identification

Multi-Channel blind system identification (MBSI) is a system identification method for identifying a multi-channel system with a common unknown input. This method is really advantageous in the systems such as human's artery that measuring the input signals are difficult but the outputs of the system in different channels can easily reach by different sensors. This method is able to identify the dynamic of each channel and estimate the unknown input signal of the system [35]. Therefore, in this type of the system, the identification algorithm is blind to the input signal.

Traditionally this method is used in communications communities [43] and image processing [44]. The limitation of this method is that it couldn't apply to the channels with common dynamic or simply the channels shouldn't have joint poles and zeros [40]. And more recently, this method has been applied in some biomedical applications such as cardiovascular monitoring [38], [40], [41]–[43]. Hahn et al. showed that this method can be applied in estimating the aortic BP waveform by means of measuring BP waves at two distinct peripheral locations [35].

Since both channels are excited with a common input by canceling the unknown input we can form:

$$G_1^{-1}(s)y_1(s) = G_2^{-1}(s)y_2(s) \tag{2-3}$$

which can be solved to derive the unknown subject-specific parameters in the arterial line models $G_1(s)$ and $G_2(s)$ via, e.g., numerical optimization in the time domain [14]:

$$\theta^* = \arg\min_{\theta} \| \mathcal{L}^{-1}[G_1^{-1}(s,\theta)y_1(s) - G_2^{-1}(s,\theta)y_2(s)] \| \tag{2-4}$$

where $\mathcal{L}$ is the Laplace transform operator and θ^* is the set of subject-specific model parameter. Hahn et al. have driven the conditions that the system with the dynamic formulation of Eq. (2-1) needs in order to all the parameters being identifiable using Eq. (2-4) [35].

2.4. De-convolution Filtering

Input de-convolution is the process of estimating the unknown input of a multi-channel system from its output measurement and the channel dynamics. Once the dynamic properties of the multi-channel system have been identified, the unknown input signal can be restored by means of de-convoluting the measured output signals.

One simple way for the systems with the invertible transfer function (stable invert transfer function with stable zeros locations) is filtering with that invert transfer function [14], [45]. However, other techniques are required when the inverted transfer function is not stable, such as direct inverse filtering least-squares and maximum-likelihood-type de-convolution [37], [46], and the design of dedicated de-convolution filters [35], [47].

Direct inverse filtering has been a straightforward choice due to the non-minimum phase nature of the channel dynamics associated with the BP wave propagation in the arteries [48]. The least-squares and maximum likelihood-type de-convolution techniques were developed primarily for finite impulse response (FIR) channel dynamics [49], [50]. Hence, central aortic BP de-convolution based on these techniques involved the FIR filter approximation of the BP propagation channel dynamics [37], [46]. To relax such restrictions, design methodologies for the input de-convolution filters applicable to coprime multi-channel systems with infinite impulse response (IIR) channel dynamics have been developed [35], [47], [51]. However, all these techniques have a common critical weakness: the integrity of input de-convolution hinges upon the accuracy of the channel dynamics. Considering that the channel dynamics themselves are estimated from output signal measurements of the system as part of the blind system identification methodology, the quality of the de-convolved input signal may be susceptible to the errors associated with the channel dynamics.

Model-Based Blind System Identification Approach to Estimation of Central Aortic Blood Pressure Waveform from Non-Invasive Diametric Circulatory Signals

Chapter 3:

3.1. Introduction

In section 2.1 the current methods for estimating central BP waveform from invasive peripheral BP measurements have been explained. However, extending these techniques to estimate central aortic BP waveform from non-invasive circulatory signals add complexity. First, low-cost non-invasive circulatory signal instruments are common in today's clinical practice (such as occlusive cuffs and pulse oximeters) measure arterial blood volume, which is morphologically different from arterial BP. Second, there are mechanics associated with the instruments, such as the pressure-volume relationship of the occlusive cuff [52] that may further change the morphology of arterial BP. Therefore, viscoelasticity of the arterial wall and tissues as well as instrument mechanics must be considered into the system identification procedure before central aortic BP waveform can be estimated from non-invasive circulatory signals.

In this chapter, a model-based blind system identification technique to estimate central aortic blood pressure waveform from non-invasive diametric circulatory signals is proposed. First, a mathematical model is driven to formulate the relationship between central aortic blood pressure waveform and a class of non-invasive circulatory signals at diametric locations. This is achieved by combining models of wave propagation in the artery, arterial pressure-volume relationship, and mechanics of the measurement instrument. Second, the problem of estimating central aortic blood pressure waveform from non-invasive diametric circulatory signals is formulated into a blind system identification problem. Third, we performed identifiability analysis to show that, in theory, the mathematical model could be identified, and its parameters determined up to an unknown scale. Finally, we illustrated the feasibility of the approach by applying it to estimate central aortic blood pressure waveform from two diametric PVR signals.

3.2. Mathematical Model of Central Aortic BP and Non-Invasive BP

The mathematical model to represent the relationship between central aortic BP and non-invasive diametric circulatory signals is made up of a tube-load model of BP wave propagation and reflection in the artery [41], a viscoelastic model to formulate the pressure-volume relationship of the arterial wall and tissue, and a mechanical model of the instrument. The overall model is shown in Figure 3-1.

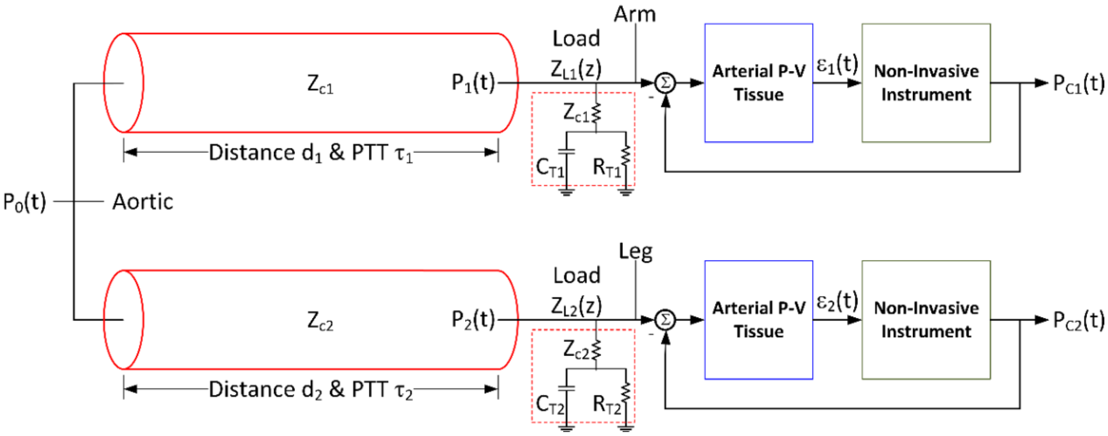

Figure 3-1-Mathematical model to reproduce the relationship between central aortic BP and non-invasive diametric circulatory signals.

The tube load model is formulated as Eq. (2-1) and the reflection coefficient in Eq. (2-2) can be expanded in Eq. (3-1).

$$\Gamma_i(z) = \frac{Z_{Li}(z) - Z_{ci}}{Z_{Li}(z) + Z_{ci}} = \frac{G_i(z)}{F_i(z)} \tag{3-1}$$

where $G_i(z) = \sum_{l=0}^{r_i} g_{l,i} z^l$ and $F_i(z) = z^{s_i} + \sum_{l=0}^{s_i-1} f_{l,i} z^l$ ($s_i \geq r_i$) are polynomials in z. The majority of work on tube-load modeling of the artery suggests that a simple resistive load (in which case $\Gamma_i(z) = g_{0,i}$) and the Windkessel load (in which case $\Gamma_i(z) = \frac{g_{0,i}}{z+f_{0,i}}$; see Figure 3-1) are enough to represent $Z_{Li}(z)$ [41]. Second, the viscoelastic model is expressed as a rational transfer function model relating the strain response $\varepsilon_i(t)$ of the artery and tissue at the distal site i to the trans-mural pressure (given by the difference between the arterial BP $P_i(t)$ and external pressure $P_{Ci}(t)$ loaded by the instrument) acting on the artery:

$$\mathcal{Z}[\varepsilon_i(t)] = \frac{N_i(z)}{D_i(z)} \mathcal{Z}[P_i(t) - P_{Ci}(t)] \tag{3-2}$$

where $N_i(z) = s^{m_i} + \sum_{l=0}^{m_i-1} b_{l,i} z^l$ and $D_i(z) = \sum_{l=0}^{n_i} a_{l,i} z^l$ ($n_i \geq m_i$) are polynomials in z. Here, we consider a class of mechanistic models that can be expressed in the following parametric form:

$$\varepsilon_i(t) = \sum_{l=1}^{N_i} c_{l,i} \psi_{l,i}[P_{Ci}(t)] \tag{3-3}$$

where $c_{l,i}$, $l = 1, \cdots, N_i$ are unknown coefficients and $\psi_{l,i}[\cdot]$, $l = 1, \cdots, N_i$ are known basis functions of the argument.

Combining all these equations, the mathematical model relating $P_{Ci}(t)$ to $P_0(t)$ is given by the following expression:

$$\mathcal{Z}[P_0(t)] = \frac{z^{\tau_i} + z^{-\tau_i}\Gamma_i(z)}{1 + \Gamma_i(z)} \left\{ \mathcal{Z}[P_{Ci}(t)] + \frac{D_i(z)}{N_i(z)} \mathcal{Z}\left[\sum_{l=1}^{N_i} c_{l,i} \psi_{l,i}[P_{Ci}(t)] \right] \right\} \tag{3-4}$$

3.3. Blind System Identification Formulation

Based on Eq. (3-4), the problem of estimating central aortic BP from non-invasive diametric circulatory signals can be formulated into a blind system identification problem in which

(i) The mathematical models in Eq. (3-4) associated with two diametric sites are identified from the measurements of $P_{Ci}(t)$, $i = 1{,}2$.

(ii) Central aortic BP waveform is estimated by filtering $P_{Ci}(t)$, $i = 1{,}2$ with the identified models in the form of Eq. (3-4).

To determine the models (specifically, unknown subject-specific parameters therein), the following correlation equation between $P_{C1}(t)$ and $P_{C2}(t)$ can be derived by canceling out $\mathcal{Z}[P_0(t)]$ from Eq. (3-4) and using (2-3):

$$\begin{aligned} &\frac{z^{\tau_1} + z^{-\tau_1}\Gamma_1(z,\theta_1)}{1+\Gamma_1(z,\theta_1)}\left\{\mathcal{Z}[P_{C1}(t)] + \frac{D_1(z,\theta_1)}{N_1(z,\theta_1)}\mathcal{Z}[\bar{\psi}_1(t,\theta_1)]\right\} \\ &\qquad = \frac{z^{\tau_2} + z^{-\tau_2}\Gamma_2(z,\theta_2)}{1+\Gamma_2(z,\theta_2)}\left\{\mathcal{Z}[P_{C2}(t)]\right. \\ &\qquad \left. + \frac{D_2(z,\theta_2)}{N_2(z,\theta_2)}\mathcal{Z}[\bar{\psi}_2(t,\theta_2)]\right\} \end{aligned} \tag{3-5}$$

where $\bar{\psi}_i(t,\theta_i) = \sum_{l=1}^{N_i} c_{l,i}\psi_{l,i}[P_{Ci}(t)]$, $i = 1{,}2$, and θ_i, $i = 1{,}2$ are the sets of unknown subject-specific polynomial parameters in Eq. (3-4) associated with the distal site i. Hence, the system identification problem reduces to the following minimization problem based on Eq. (2-4) with the following objective function:

$$\Theta^* = \arg\min_{\Theta} \|P_0(t,\Theta_1) - P_0(t,\Theta_2)\| \tag{3-6}$$

where $\Theta = \{\Theta_1, \Theta_2\}$ is the set of subject-specific model parameters, $\Theta_i = \{\tau_i, \theta_i\}$, $\theta_i = \{f_{0,i} \cdots f_{s_i-1,i}, g_{0,i} \cdots g_{r_i,i}, a_{0,i} \cdots a_{n_i,i}, b_{0,i} \cdots b_{m_i-1,i}\}$, $i = 1{,}2$, Θ^* the optimal value of

Θ, and $P_0(t,\Theta_i) = \mathcal{Z}^{-1}\left[\frac{z^{\tau_i}+z^{-\tau_i}\Gamma_i(z,\theta_i)}{1+\Gamma_i(z,\theta_i)}\left\{\mathcal{Z}[P_{Ci}(t)] + \frac{D_i(z,\theta_i)}{N_i(z,\theta_i)}\mathcal{Z}[\bar{\psi}_i(t,\theta_i)]\right\}\right]$, $i = 1{,}2$ the central aortic BP waveforms estimated from $P_{Ci}(t)$ and the corresponding models in the form of Eq. (3-4).

3.4. Parametric Identifiability Analysis

First, we need to ensure that all the parameters in Θ (Eq. (3-6)) are identifiable (in other words, that they can be uniquely determined). To examine the identifiability of the parameters in Θ, Eq. (3-5) can be rewritten into an equivalent algebraic equation that can be solved using the least-squares technique. Using Eq. (3-1), Eq. (3-5) can be rewritten as follows:

$$\begin{aligned} &H_{11}(z,\Theta)\mathcal{Z}[P_{C1}(t)] + H_{12}(z,\Theta)\mathcal{Z}[\bar{\psi}_1(t,\theta_1)] \\ &\qquad = H_{21}(z,\Theta)\mathcal{Z}[P_{C2}(t)] + H_{22}(z,\Theta)\mathcal{Z}[\bar{\psi}_2(t,\theta_2)] \end{aligned} \tag{3-7}$$

where $H_{11}(z,\Theta)$, $H_{12}(z,\Theta)$, $H_{21}(z,\Theta)$ and $H_{22}(z,\Theta)$ are given by:

$$\begin{aligned} H_{11}(z,\Theta) &= [z^{\tau_1}F_1(z,\theta_1) + z^{-\tau_1}G_1(z,\theta_1)][F_2(z,\theta_2) \\ &\qquad + G_2(z,\theta_2)]N_1(z,\theta_1)N_2(z,\theta_2) \\ H_{12}(z,\Theta) &= [z^{\tau_1}F_1(z,\theta_1) + z^{-\tau_1}G_1(z,\theta_1)][F_2(z,\theta_2) \\ &\qquad + G_2(z,\theta_2)]D_1(z,\theta_1)N_2(z,\theta_2) \\ H_{21}(z,\Theta) &= [z^{\tau_2}F_2(z,\theta_2) + z^{-\tau_2}G_2(z,\theta_2)][F_1(z,\theta_1) \\ &\qquad + G_1(z,\theta_1)]N_1(z,\theta_1)N_2(z,\theta_2) \\ H_{22}(z,\Theta) &= [z^{\tau_2}F_2(z,\theta_2) + z^{-\tau_2}G_2(z,\theta_2)][F_1(z,\theta_1) \\ &\qquad + G_1(z,\theta_1)]N_1(z,\theta_1)D_2(z,\theta_2) \end{aligned} \tag{3-8}$$

Considering that $F_i(z,\theta_i)$ is monic and $s_i = \deg F_i(z) \geq \deg G_i(z) = r_i$, it can be concluded that $[z^{\tau_i}F_i(z,\theta_i) + z^{-\tau_i}G_i(z,\theta_i)]$ and $[F_i(z,\theta_i) + G_i(z,\theta_i)]$ are also monic.

Further, considering that $N_i(z,\theta_i)$, $i=1{,}2$ are monic, it can be concluded that $H_{11}(z,\Theta)$ and $H_{21}(z,\Theta)$ are also monic. However, $H_{12}(z,\Theta)$ and $H_{22}(z,\Theta)$ are not monic, since $D_i(z,\theta_i)$, $i=1{,}2$ are not monic. Indeed, expanding these polynomials yields:

$$\begin{aligned}
H_{11}(z,\Theta) &= \sum_{k=-\tau_1}^{\tau_1+s_1+s_2+m_1+m_2} h_k^{(11)} z^k \\
&= z^{\tau_1+s_1+s_2+m_1+m_2} + \cdots + g_{0,1}\big(f_{0,2}+g_{0,2}\big)b_{0,1}b_{0,2}z^{-\tau_1} \\
H_{12}(z,\Theta) &= \sum_{k=-\tau_1}^{\tau_1+s_1+s_2+n_1+m_2} h_k^{(12)} z^k \\
&= a_{n_1,1}z^{\tau_1+s_1+s_2+n_1+m_2} + \cdots + g_{0,1}\big(f_{0,2}+g_{0,2}\big)a_{0,1}b_{0,2}z^{-\tau_1} \\
H_{21}(z,\Theta) &= \sum_{k=-\tau_2}^{\tau_2+s_1+s_2+m_1+m_2} h_k^{(21)} z^k \\
&= z^{\tau_2+s_1+s_2+m_1+m_2} + \cdots + g_{0,2}\big(f_{0,1}+g_{0,1}\big)b_{0,1}b_{0,2}z^{-\tau_2} \\
H_{22}(z,\Theta) &= \sum_{k=-\tau_2}^{\tau_2+s_1+s_2+m_1+n_2} h_k^{(22)} z^k \\
&= a_{n_2,2}z^{\tau_2+s_1+s_2+m_1+n_2} + \cdots + g_{0,2}\big(f_{0,1}+g_{0,1}\big)a_{0,2}b_{0,1}z^{-\tau_2}
\end{aligned} \tag{3-9}$$

Finally, Eq. (3-7) can be transformed into the following algebraic equation by exploiting Eq. (3-9) and the time series sequences of $P_{Ci}(t)$, $i=1{,}2$:

$$P_{C1}(t+\tau_1+s_1+s_2+m_1+m_2)-P_{C2}(t+\tau_2+s_1+s_2+m_1+m_2)$$

$$=[-\boldsymbol{\phi}_{\mathbf{0},\mathbf{1}}(t) \quad -\boldsymbol{\phi}_{\mathbf{1},\mathbf{1}}(t) \quad \cdots \quad -\boldsymbol{\phi}_{\boldsymbol{N_1},\mathbf{1}}(t) \quad \boldsymbol{\phi}_{\mathbf{0},\mathbf{2}}(t) \quad \boldsymbol{\phi}_{\mathbf{1},\mathbf{2}}(t) \quad \cdots \quad \boldsymbol{\phi}_{\boldsymbol{N_2},\mathbf{2}}(t)]\begin{bmatrix} \boldsymbol{h}_{\mathbf{11}} \\ c_{1,1}\boldsymbol{h}_{\mathbf{12}} \\ \vdots \\ c_{N_1,1}\boldsymbol{h}_{\mathbf{12}} \\ \boldsymbol{h}_{\mathbf{21}} \\ c_{1,2}\boldsymbol{h}_{\mathbf{22}} \\ \vdots \\ c_{N_2,2}\boldsymbol{h}_{\mathbf{22}} \end{bmatrix}$$

(3-10a)

where

$$\boldsymbol{\phi}_{\mathbf{0},\boldsymbol{i}}(t)=[P_{ci}(t+\tau_i+s_1+s_2+m_1+m_2-1) \quad \cdots \quad P_{ci}(t-\tau_i)], i$$
$$=1,2$$

$$\boldsymbol{\phi}_{\boldsymbol{l},\mathbf{1}}(t)$$
$$=[\psi_{l,1}[P_{C1}(t+\tau_1+s_1+s_2+n_1+m_2)] \quad \cdots \quad \psi_{l,1}[P_{C1}(t-\tau_1)]],$$
$$l=1,\cdots,N_1$$

(3-10b)

$$\boldsymbol{\phi}_{\boldsymbol{l},\mathbf{2}}(t)$$
$$=[\psi_{l,2}[P_{C2}(t+\tau_2+s_1+s_2+m_1+n_2)] \quad \cdots \quad \psi_{l,2}[P_{C1}(t-\tau_2)]],$$
$$l=1,\cdots,N_2$$

and

$$\boldsymbol{h}_{\boldsymbol{i}\mathbf{1}}=\left[h^{(i1)}_{\tau_i+s_1+s_2+m_1+m_2-1} \quad \cdots \quad h^{(i1)}_{-\tau_i}\right]^{\mathrm{T}}, \qquad i=1,2$$

$$\boldsymbol{h}_{\mathbf{12}}=\left[h^{(12)}_{\tau_1+s_1+s_2+n_1+m_2} \quad \cdots \quad h^{(12)}_{-\tau_1}\right]^{\mathrm{T}}$$

(3-10c)

$$\boldsymbol{h}_{\mathbf{22}}=\left[h^{(22)}_{\tau_2+s_1+s_2+m_1+n_2} \quad \cdots \quad h^{(22)}_{-\tau_2}\right]^{\mathrm{T}}$$

Theorem 1: Consider the blind system identification problem in Eq. (3-6) which can be cast into the algebraic equation in Eq. (3-10a). Assume that τ_i, $i=1,2$ are known and that $G_i(z,\theta_i)=g_{0,i}$, $i=1,2$. If the diametric circulatory signal measurement sites are chosen so that the following conditions on PTT τ_i, $i = 1{,}2$ are satisfied:

$$\begin{aligned} &2\tau_1 \geq \max(s_2 + m_1 + m_2, s_2 + n_1 + m_2) + 1 \\ &2\tau_2 \geq \max(s_1 + m_1 + m_2, s_1 + m_1 + n_2) + 1 \end{aligned} \tag{3-11}$$

then (i) the tube-load models in Eq. (2-1) are identifiable, while (ii) the viscoelastic models in Eq. (3-2) and the mechanistic non-invasive instrument models in Eq. (3-3) are identifiable up to an unknown scale.

Proof: Using the time series sequences of $P_{Ci}(t)$, $i = 1{,}2$ and $1 \leq t \leq N$ where N is the length of the time series sequences, Eq. (3-10a) can be rewritten into the following matrix equation:

$$\underbrace{\begin{bmatrix} P_{c1}(1 + \tau_1 + s_1 + s_2 + m_1 + m_2) - P_{C2}(1 + \tau_2 + s_1 + s_2 + m_1 + m_2) \\ \vdots \\ P_{c1}(N + \tau_1 + s_1 + s_2 + m_1 + m_2) - P_{C2}(N + \tau_2 + s_1 + s_2 + m_1 + m_2) \end{bmatrix}}_{\mathbf{Y}}$$

$$= \underbrace{\begin{bmatrix} -\boldsymbol{\phi}_{\mathbf{0,1}}(1) & -\boldsymbol{\phi}_{\mathbf{1,1}}(1) & & -\boldsymbol{\phi}_{\boldsymbol{N_1},\mathbf{1}}(1) & \boldsymbol{\phi}_{\mathbf{0,2}}(1) & \boldsymbol{\phi}_{\mathbf{1,2}}(1) & & \boldsymbol{\phi}_{\boldsymbol{N_2},\mathbf{2}}(1) \\ \vdots & \vdots & \cdots & \vdots & \vdots & \vdots & \cdots & \vdots \\ -\boldsymbol{\phi}_{\mathbf{0,1}}(N) & -\boldsymbol{\phi}_{\mathbf{1,1}}(N) & & -\boldsymbol{\phi}_{\boldsymbol{N_1},\mathbf{1}}(N) & \boldsymbol{\phi}_{\mathbf{0,2}}(N) & \boldsymbol{\phi}_{\mathbf{1,2}}(N) & & \boldsymbol{\phi}_{\boldsymbol{N_2},\mathbf{2}}(N) \end{bmatrix}}_{\mathbf{\Phi}} \begin{bmatrix} \boldsymbol{h}_{\mathbf{11}} \\ c_{1,1}\boldsymbol{h}_{\mathbf{12}} \\ \vdots \\ c_{N_1,1}\boldsymbol{h}_{\mathbf{12}} \\ \boldsymbol{h}_{\mathbf{21}} \\ c_{1,2}\boldsymbol{h}_{\mathbf{22}} \\ \vdots \\ c_{N_2,2}\boldsymbol{h}_{\mathbf{22}} \end{bmatrix} \tag{3-12}$$

The solution $[\boldsymbol{h}_{\mathbf{11}}^* \quad c_{1,1}^*\boldsymbol{h}_{\mathbf{12}}^* \quad \cdots \quad c_{N_1,1}^*\boldsymbol{h}_{\mathbf{12}}^* \quad \boldsymbol{h}_{\mathbf{21}}^* \quad c_{1,2}^*\boldsymbol{h}_{\mathbf{22}}^* \quad \cdots \quad c_{N_2,2}^*\boldsymbol{h}_{\mathbf{22}}^*]$ to Eq. (3-12) is given by the least-squares technique as $(\mathbf{\Phi}^{\mathrm{T}}\mathbf{\Phi})^{-1}\mathbf{\Phi}\mathbf{Y}$. From $\boldsymbol{h}_{\mathbf{11}}^*$ and $\boldsymbol{h}_{\mathbf{21}}^*$ thus identified, $H_{11}(z, \Theta^*)$ and $H_{21}(z, \Theta^*)$ can be constructed using Eq. (3-9). Now, according to Theorem 1 presented in Hahn et al. [35], the conditions in Eq. (3-11) dictate that these polynomials can be decomposed as follows:

$$H_{11}(z,\Theta^*) \rightarrow [z^{\tau_1}F_1(z,\theta_1^*) + z^{-\tau_1}G_1(z,\theta_1^*)] \text{ and } [F_2(z,\theta_2^*) + G_2(z,\theta_2^*)]N_1(z,\theta_1^*)N_2(z,\theta_2^*)$$

$$H_{21}(z,\Theta^*) \rightarrow [z^{\tau_2}F_2(z,\theta_2^*) + z^{-\tau_2}G_2(z,\theta_2^*)] \text{ and } [F_1(z,\theta_1^*) + G_1(z,\theta_1^*)]N_1(z,\theta_1^*)N_2(z,\theta_2^*) \tag{3-13}$$

Then, the polynomials $F_i(z,\theta_i^*)$ and $G_i(z,\theta_i^*)$ can be determined from $[z^{\tau_i}F_i(z,\theta_i^*) + z^{-\tau_i}G_i(z,\theta_i^*)]$, $i = 1,2$. In this way, the tube-load models can be determined via Eq. (2-1) and (3-1). Also, noting that $c_{l,i}^*\boldsymbol{h}_{i2}^*$, $i = 1,2$ and $1 \le l \le N_i$ identified from Eq. (3-12) can be written as follows:

$$[c_{1,i}^*\boldsymbol{h}_{i2}^* \quad \cdots \quad c_{N_i,i}^*\boldsymbol{h}_{i2}^*] = \boldsymbol{h}_{i2}^*[c_{1,i}^* \quad \cdots \quad c_{N_i,i}^*] \tag{3-14}$$

the vectors $\boldsymbol{h}_{i2}^*$ and $[c_{1,i}^* \quad \cdots \quad c_{N_i,i}^*]$ can be determined (up to an unknown scale) from $c_{l,i}^*\boldsymbol{h}_{i2}^*$, $i = 1,2$ and $1 \le l \le N_i$ as the left singular vector and right singular vector of the matrix $[c_{1,i}^*\boldsymbol{h}_{i2}^* \quad \cdots \quad c_{N_i,i}^*\boldsymbol{h}_{i2}^*]$ associated with the maximum singular value . In this way, the vector $[c_{1,i}^* \quad \cdots \quad c_{N_i,i}^*]$ determines the mechanistic non-invasive instrument models in Eq. (3-3) (up to an unknown scale). In addition, from $\boldsymbol{h}_{12}^*$ and $\boldsymbol{h}_{22}^*$ thus identified (up to an unknown scale), $H_{12}(z,\Theta^*)$ and $H_{22}(z,\Theta^*)$ can be constructed using Eq. (3-9) (up to an unknown scale). Now again, according to Theorem 1 presented in Hahn et al. [35], the conditions in Eq. (3-11) dictate that these polynomials can be decomposed as follows:

$$H_{12}(z,\Theta^*) \rightarrow \tag{3-15}$$

$$[z^{\tau_1}F_1(z,\theta_1^*) + z^{-\tau_1}G_1(z,\theta_1^*)] \text{ and } [F_2(z,\theta_2^*) + G_2(z,\theta_2^*)]D_1(z,\theta_1^*)N_2(z,\theta_2^*)$$

$H_{22}(z,\Theta^*) \rightarrow$

$$[z^{\tau_2}F_2(z,\theta_2^*) + z^{-\tau_2}G_2(z,\theta_2^*)] \text{ and } [F_1(z,\theta_1^*) + G_1(z,\theta_1^*)]N_1(z,\theta_1^*)D_2(z,\theta_2^*)$$

Here, the unknown scale is imposed on $D_i(z,\theta_i^*)$, $i = 1,2$ since the remaining polynomials $[z^{\tau_i}F_i(z,\theta_i^*) + z^{-\tau_i}G_i(z,\theta_i^*)]$, $[F_i(z,\theta_i^*) + G_i(z,\theta_i^*)]$ and $N_i(z,\theta_1^*)$, $i = 1,2$ constituting $H_{12}(z,\Theta^*)$ and $H_{22}(z,\Theta^*)$ are all monic. Finally, the viscoelastic models in Eq. (3-2) can be determined (up to an unknown scale) from the polynomials decomposed in Eq. (3-13) and Eq. (3-15) as follows:

$$\frac{N_1(z,\theta_1^*)}{D_1(z,\theta_1^*)} = \frac{[F_2(z,\theta_2^*) + G_2(z,\theta_2^*)]N_1(z,\theta_1^*)N_2(z,\theta_2^*)}{[F_2(z,\theta_2^*) + G_2(z,\theta_2^*)]D_1(z,\theta_1^*)N_2(z,\theta_2^*)}$$
$$\frac{N_2(z,\theta_2^*)}{D_2(z,\theta_2^*)} = \frac{[F_1(z,\theta_1^*) + G_1(z,\theta_1^*)]N_1(z,\theta_1^*)N_2(z,\theta_2^*)}{[F_1(z,\theta_1^*) + G_1(z,\theta_1^*)]N_1(z,\theta_1^*)D_2(z,\theta_2^*)} \tag{3-16}$$

Remark 1: The condition in Eq. (3-11) can be easily satisfied by appropriate selection of measurement locations Since longer channel distance increase the PTT and sampling rate [35].

Remark 2: Eq. (3-4) indicates that the values of PTT τ_i, $i = 1,2$ are related to the model structure. Since PTT is not linearly parameterized in Eq. (3-10a), establishing the identifiability of PTT is not trivial. However, it has been illustrated that PTT may be reliably found via exhaustive search [14], [54], [55]. For this model, Eq. (3-6) was solved for multiple candidate PTTs and the solution attaining the minimum cost function in Eq. (3-6) was taken as the optimal PTTs.

Remark 3: Considering that simple resistive or Windkessel load is sufficient for the purpose of tube-load modeling of the artery, the assumption of $G_i(z, \theta_i) = g_{0,i}$, $i = 1,2$ is appropriate at least in the context of the problem considered here.

Remark 4: Theorem 1 indicates that the minimization problem in Eq. (3-6) is basically underdetermined. Specifically, Eq. (3-5) is not altered by scaling $D_i(z, \theta_i)$ to $\alpha D_i(z, \theta_i)$ and $[c_{1,i} \quad \cdots \quad c_{N_i i}]$ to $\frac{1}{\alpha}[c_{1,i} \quad \cdots \quad c_{N_i i}]$ (because the scaling factors cancel each other). To make the problem well-posed, a subset of parameters must be known a priori or fixed at constant values. For example, fixing $a_{n_i,i}$, $i = 1,2$ to unity makes Eq. (3-6) well-posed by making $H_{12}(z, \Theta)$ and $H_{22}(z, \Theta)$ monic (see Eq. (3-8) and (3-9)).

Remark 5: It is important to mention that the scale of the estimated central aortic BP waveform is not affected by the undetermined scales associated with the viscoelastic ((3-2)) and mechanistic ((3-3)) models. Considering Eq. (3-10a), $c_{l,i}^* \boldsymbol{h}_{i2}^*$, $i = 1,2$ and $l = 1 \leq l \leq N_i$ can be obtained by any combination of $\alpha c_{l,i}^*$ and $\frac{1}{\alpha} \boldsymbol{h}_{i2}^*$ where α is the unknown scale. According to Eq. (3-15) , $\frac{1}{\alpha} \boldsymbol{h}_{i2}^*$ leads to $\frac{1}{\alpha} D_i(z, \theta_i^*)$ since all the remaining polynomials constituting $H_{i2}(z, \Theta^*)$ are monic. Now, Eq. (3-4) indicates that the scale of $P_0(t)$ is not influenced by this scale uncertainty because the unknown scaling factor α is eliminated while $\frac{D_i(z)}{N_i(z)}$ is multiplied to $\mathcal{Z}[\bar{\psi}_i(t, \theta_i^*)]$.

3.5. Estimation of Central Aortic BP Wave from Diametric PVR Signals via Blind System Identification

To validate the proposed technique, the problem of estimating central aortic BP waveform from two diametric PVR signals acquired from an arm and a leg is considered. First, the mathematical model is formulated based on the relationship between central aortic BP and distal PVR, and a viscoelastic model is selected for the arm and leg to be used in the MBSI problem. Second, this proposed MBSI approach is formulated and validated.

3.5.1. Experimental Protocol

Data is collected from 10 cardiac catheterization patients at the University of Maryland Medical Center under IRB approval and written informed consent. Invasive central aortic BP waveform was measured with a catheter inserted via a femoral artery per routine standard of care. PVR signals were measured with occlusive cuffs (TSD120, Biopac Systems, CA, USA) placed around an upper arm and an upper leg. The cuffs were inflated to a sub-diastolic level of ~10 mmHg below DP measured with the central aortic catheter. These simultaneously measured waveform data were stored in a laptop computer via a data acquisition system (MP150, Biopac Systems, CA, USA) at a sampling rate of 1 kHz for ~1 min. The data acquisition system was properly calibrated before the beginning of each data collection to assure that accurate BP waveform data were collected. During the data collection, the mean arterial BP (MAP) of the subjects ranged 94.6±20.1 mmHg (mean±SD), and the waveform morphology was physiologic in all the subjects.

3.5.2. Mathematical Modeling, Validation, and Model Structure Selection

A lossless tube-load model terminated with a Windkessel load is considered as the model of BP wave propagation and reflection in the artery (see Figure 3-1). And the Windkessel load $\Gamma_i(z) = \frac{g_{0,i}}{z+f_{0,i}}$ is considered for Eq. (2-1) which leads to the following tube-load model associated with the distal site i:

$$\mathcal{Z}[P_i(t)] = \frac{z + f_{0,i} + g_{0,i}}{z^{\tau_i+1} + f_{0,i} z^{\tau_i} + g_{0,i} z^{-\tau_i}} \mathcal{Z}[P_0(t)] \tag{3-17}$$

We considered the constant gain, Voigt and SLS models as the viscoelastic models to relate the diametric trans-mural pressure waveforms (arterial BP waveforms minus PVR signals) to the corresponding strain of the artery and tissue.

For the Voigt model, the transfer function is given by:

$$\mathcal{Z}[\varepsilon_i(t)] = \frac{1}{a_{1,i} z + a_{0,i}} \mathcal{Z}[P_i(t) - P_{Ci}(t)] \tag{3-18}$$

while the SLS model is given by:

$$\mathcal{Z}[\varepsilon_i(t)] = \frac{z + b_{0,i}}{a_{1,i} z + a_{0,i}} \mathcal{Z}[P_i(t) - P_{Ci}(t)] \tag{3-19}$$

We developed a mechanistic model of the occlusive cuff as follows. This model is shown in Figure 3-2 where $P_i(t)$: arterial BP at the distal site i. $\varepsilon_i(t)$: pulsation of the arterial wall at the distal site i. $P_{Ci}(t)$: PVR signal at the distal site i. $V_{Ci}(t)$: volume of the air in the cuff at the distal site i.

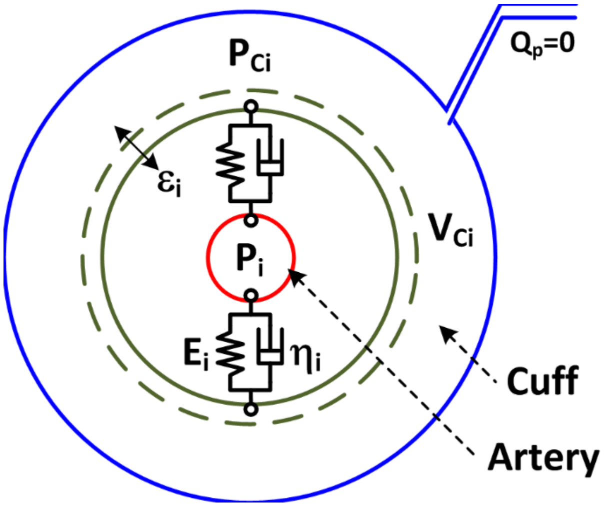

Figure 3-2- Mechanistic model of an occlusive cuff. (Here, the Voigt model is shown as the viscoelastic model of the arterial wall for simplicity of illustration)

Consider the assumption that the expansion of the external wall of the occlusive cuff in response to the pulsation of the arterial wall $\varepsilon_i(t)$ is negligible, the volume $V_{Ci}(t)$ of the air in the occlusive cuff (which has been inflated to a sub-DP level and isolated) is determined by $\varepsilon_i(t)$. The change in $V_{Ci}(t)$, $\delta V_{Ci}(t)$, in response to $\varepsilon_i(t)$ is calculated by:

$$V_{Ci} = \pi L \breve{r}_i^2 \left(1 + \varepsilon_i(t)\right)^2 \tag{3-20}$$

$$\begin{aligned} \delta V_{Ci}(t) = V_{Ci} - \breve{V}_i &= -\left(\pi\, L\, \breve{r}_i^2\, \left(1 + \varepsilon_i(t)\right)^2 - \pi\, L\, \breve{r}_i^2\right) \\ &= \breve{V}_i \left[1 - \left(1 + \varepsilon_i(t)\right)^2\right] \end{aligned} \tag{3-21}$$

where L and $\breve{r}_i$ are the length and the initial radius of it and $\breve{V}_i$ is the volume of the air in the occlusive cuff when the arterial BP is almost equal to DP. If we model the pressure-volume relationship of the occlusive cuff by way of the Boyle’s law [56], $P_{Ci}(t)$ can be expressed by $\delta V_{Ci}(t)$ as follows, where $\breve{P}_i$ is the pressure of the air in the occlusive cuff when the arterial BP is equal to DP:

$$\begin{aligned} &\left(\breve{P}_i + P_{atm}\right)\breve{V}_i = \left(P_{Ci}(t) + P_{atm}\right)\left[\breve{V}_i + \delta V_{Ci}(t)\right] \\ &\rightarrow P_{Ci}(t) = \frac{\left(\breve{P}_i + P_{atm}\right)\breve{V}_i}{\left[\breve{V}_i + \delta V_{Ci}(t)\right]} - P_{atm} \end{aligned} \tag{3-22}$$

Finally, the mechanistic model of the occlusive cuff relating $\varepsilon_i(t)$ to $P_{Ci}(t)$ is obtained by combining Eq. (3-21) and Eq. (3-22):

$$\varepsilon_i(t) = \sqrt{2 - \frac{\breve{P}_i + P_{atm}}{P_{Ci}(t) + P_{atm}}} - 1 \tag{3-22}$$

This mechanistic model is a special case of Eq. (3-3) which does not involve any unknown coefficients ($\breve{P}_i$ is the sub-DP level, which is known).

Combining the models in Eq. (3-17) - (3-22) yields the following mathematical model for the relationship between central aortic BP waveform and a distal PVR signal (where $a_{1,i}, b_{1,i} = 0$ and $b_{0,i} = 1$ in case of constant gain, $b_{1,i} = 0$ and $b_{0,i} = 1$ in case of the Voigt model while $b_{1,i} = 1$ and unknown $b_{1,i}$ in case of the SLS model):

$$\begin{aligned}\mathcal{Z}[P_0(t)] = \frac{z^{\tau_i+1} + f_{0,i} z^{\tau_i} + g_{0,i} z^{-\tau_i}}{z + f_{0,i} + g_{0,i}} \Bigg\{ & \mathcal{Z}[P_{Ci}(t)] \\ & + \frac{a_{1,i} z + a_{0,i}}{b_{1,i} z + b_{0,i}} \mathcal{Z}\left[\sqrt{2 - \frac{\breve{P}_i + P_{atm}}{P_{Ci}(t) + P_{atm}}} - 1\right]\Bigg\}\end{aligned} \tag{3-23}$$

The validity of this model is studied using the collected experimental data explained in section 3.5.1. Next step was to determine appropriate viscoelastic model in Eq. (3-23) associated with the arm and leg. For both arm and leg, we identified the model in Eq. (3-23) considering all the three options constant gain, Voigt and SLS models using the experimental central aortic BP waveform and distal PVR signals by means of standard input-output system identification procedure similar to Rashedi et al. [54] and Abdollahzade et al. [55]. Then, the validity and relative accuracy of these models in terms of sample-by-sample root-mean-squared error (RMSE) as well as errors associated with SBP and PP are compared, all between measured central aortic BP waveform and the same waveform estimated by the identified model from distal PVR signal (see Eq. (3-23)). Finally, the best model structure (specifically viscoelastic models for the arm and leg) is chosen to be used in formulating the MBSI problem based on the qualitative and statistical comparison of the error metrics.

3.5.3. Estimation of Central Aortic BP Waveform via Blind System Identification

Using the collected experimental data and the model structure selected above (that is, the model in Eq. (3-23) with the viscoelastic models selected above), the proposed blind system identification approach is examined to estimate central aortic BP waveform from diametric PVR signals measured at an arm and a leg as follows.

First, the minimization problem in Eq. (3-6) is formulated based on the selected viscoelastic model structure. Starting with random initial estimates for the set of model parameters $\Theta = \{\Theta_1, \Theta_2\}$, $\Theta_i = \{\tau_i, \theta_i\}$, $\theta_i = \{\theta_{TL,i}, \theta_{VE,i}\}$, $\theta_{TL,i} = \{f_{0,i}, g_{0,i}\}$ (TL stands for tube-load model), $\theta_{VE,i} = \{a_{1,i}, a_{0,i}, b_{1,i}, b_{0,i}\}$ (VE stands for viscoelastic model), $i = 1{,}2$. The central aortic BP waveform $P_0(t, \Theta_i)$ in Eq. (3-6) was estimated from $P_{Ci}(t)$ using Eq. (3-23) with the selected model structure, or specifically, by (i) computing $\varepsilon_i(t)$ from $P_{Ci}(t)$ using Eq. (3-22), (ii) computing $P_i(t, \Theta_i)$,), $i = 1{,}2$, from $\varepsilon_i(t)$ and $P_{Ci}(t)$ using Eq. (3-24):

$$\mathcal{Z}[P_i(t, \Theta_i)] = \mathcal{Z}[P_{Ci}(t)] + \frac{a_{1,i}z + a_{0,i}}{b_{1,i}z + b_{0,i}}\mathcal{Z}[\varepsilon_i(t)] \tag{3-24}$$

and (iii) computing $P_0(t, \Theta_i)$, $i = 1{,}2$, using Eq. (3-17). To use the time series sequence of $P_{Ci}(t)$, $i = 1{,}2$, $P_i(t, \Theta_i)$ and $P_0(t, \Theta_i)$, $i = 1{,}2$, were computed in the discrete time domain by transforming Eq. (3-24) and Eq. (3-17) into the following difference equations:

$$P_i(t, \Theta_i) = P_{Ci}(t) + a_{0,i}\varepsilon_i(t)$$

(Gain model)

$$P_i(t, \Theta_i) = P_{Ci}(t) + a_{1,i}\varepsilon_i(t+1) + a_{0,i}\varepsilon_i(t)$$

(Voigt model)

$$P_i(t+1,\Theta_i) = -b_{0,i}P_i(t,\Theta_i) + P_{Ci}(t+1) + b_{0,i}P_{Ci}(t) + a_{1,i}\varepsilon_i(t+1) + a_{0,i}\varepsilon_i(t)$$

(SLS model)

(3-25a)

$$P_0(t+1,\Theta_i) = -\left(f_{0,i}+g_{0,i}\right)P_0(t,\Theta_i) + P_i(t+\tau_i+1,\Theta_i) + f_{0,i}P_i(t+\tau_i,\Theta_i) + g_{0,i}P_i(t-\tau_i,\Theta_i)$$

(3-26b)

Then, the minimization problem in Eq. (3-6) was solved using the time series sequences of $P_0(t,\Theta_i)$, $i = 1,2$ to determine the optimal set of parameters Θ^* (see Remark 6 for the details of how the minimization problem was actually formulated). Finally, the estimated central aortic BP waveform corresponding to Θ^* was computed as the weighted average of the two estimates $P_0(t,\Theta_1^*)$ and $P_0(t,\Theta_2^*)$:

$$P_0(t,\Theta^*) = \sigma_1 P_0(t,\Theta_1^*) + \sigma_2 P_0(t,\Theta_2^*) \tag{3-26}$$

For these results, the $\sigma_1 = \sigma_2 = 0.5$ is used.

Remark 6: Since the mathematical model does not involve unknown parameters in the mechanistic instrument model (see Eq. (3-22)), all the parameters in θ_i, $i = 1,2$ can be identified from the proposed approach (there won't be any scaling issue for this problem). In fact, Eq. (3-10a) reduces to the following algebraic equation when implemented with the models shown in Eq. (3-17)-(3-23):

$$P_{c1}(t+\tau_1+s_1+s_2+m_1+m_2) - P_{C2}(t+\tau_2+s_1+s_2+m_1+m_2) = \begin{bmatrix}-\boldsymbol{\phi}_{\mathbf{0},\mathbf{1}}(t) & -\boldsymbol{\phi}_{\mathbf{1},\mathbf{1}}(t) & \boldsymbol{\phi}_{\mathbf{0},\mathbf{2}}(t) & \boldsymbol{\phi}_{\mathbf{1},\mathbf{2}}(t)\end{bmatrix}\begin{bmatrix}\boldsymbol{h}_{\mathbf{11}}\\ \boldsymbol{h}_{\mathbf{12}}\\ \boldsymbol{h}_{\mathbf{21}}\\ \boldsymbol{h}_{\mathbf{22}}\end{bmatrix} \tag{3-27}$$

Hence, Theorem 1 dictates that both the tube-load models in Eq. (3-17) and the viscoelastic models are identifiable if the following conditions are satisfied:

$$\tau_1 \geq 2 \text{ and } \tau_2 \geq 2 \tag{3-28}$$

Though the parametric identifiability is theoretically guaranteed as discussed above, solving the minimization problem in Eq. (3-6) using experimental data is not trivial. Indeed, this identification problem contains up to 12 subject-specific parameters which should be optimized from two diametric PVR signals whose frequency contents are quite sparse (arterial circulatory waveforms typically possess energy contents at the heart rate which is normally around 0.6~1 Hz and just a few of its harmonics [24]). In addition, any modeling error associated with Eq. (3-23) adversely affects the quality of the blind system identification. To overcome the above-mentioned limitations and streamline the solution procedure, we considered the use of SBP, MP, and DBP measurements at the distal sites in solving the minimization problem in Eq. (3-6). In fact, this is a realistic idea because SBP, MP and DBP measurements can be readily obtained from occlusive cuffs by way of auscultation and/or oscillometry. By incorporating these distal BP measurements, we reformulated Eq. (3-6) into a two-stage minimization problem. In the first stage, the viscoelastic models are identified by solving the following minimization problem for each distal site using measured significant pressures:

$$\begin{aligned}\theta_{VE,i}^{*} = \arg\min_{\theta_{VE,i}} \Big\{ &\left|\hat{P}_i(t) - \hat{P}_i\big(t,\theta_{VE,i}\big)\right| + \left|\bar{P}_i(t) - \bar{P}_i\big(t,\theta_{VE,i}\big)\right| \\ &+ \left|\check{P}_i(t) - \check{P}_i\big(t,\theta_{VE,i}\big)\right| \Big\}\end{aligned} \tag{3-29}$$

where $P_i\big(t,\theta_{VE,i}\big)$, $i = 1,2$ are computed using Eq. (3-25a), and $\overset{\frown}{(\cdot)}$, $\overline{(\cdot)}$ and $\overset{\smile}{(\cdot)}$ denote SP, MP and DP. Our experimental data did not include distal SBP, MP and DBP measurements. To still show the proof-of-principle of the proposed blind system identification approach, simulated distal SBP, MAP and DBP values is employed, which were obtained by inputting distal PVR signals to the models in Eq. (3-18)-(3-22) identified from the standard input-output system identification (see 3.5.2 for details). In the second stage, the tube-load models are identified by solving the following minimization problem:

$$\begin{aligned}&\left\{\tau_1^*, \theta_{TL,1}^*, \tau_2^*, \theta_{TL,2}^*\right\}\\ &\qquad = \arg\min_{\tau_1,\theta_{TL,1},\tau_2,\theta_{TL,2}}\left[\left\|P_0\left(t,\tau_1,\theta_{TL,1}\right) - P_0\left(t,\tau_2,\theta_{TL,2}\right)\right\|\right.\\ &\qquad + \eta_1\left\|\check{P}_1(t) - \check{P}_0\left(t,\tau_1,\theta_{TL,1}\right)\right\|\\ &\qquad \left.+ \eta_2\left\|\check{P}_1(t) - \check{P}_0\left(t,\tau_2,\theta_{TL,2}\right)\right\|\right]\end{aligned} \tag{3-30}$$

where $\eta_i > 0$, $i = 1{,}2$, and $P_0\left(t,\tau_i,\theta_{TL,i}\right)$, $i = 1{,}2$ are computed using Eq. (3-31):

$$\begin{aligned}&P_0\left(t+1,\tau_i,\theta_{TL,i}\right)\\ &\qquad = -\left(f_{0,i} + g_{0,i}\right)P_0\left(t,\theta_{TL,i}\right) + P_i\left(t+\tau_i+1,\theta_{VE,i}^*\right)\\ &\qquad + f_{0,i}P_i\left(t+\tau_i,\theta_{VE,i}^*\right) + g_{0,i}P_i\left(t-\tau_i,\theta_{VE,i}^*\right)\end{aligned} \tag{3-31}$$

and $P_i\left(t,\theta_{VE,i}^*\right)$, $i = 1{,}2$ are the distal BP waveforms estimated from $P_{Ci}(t)$ using Eq. (3-22) and Eq. (3-25a) with the viscoelastic models characterized by $\theta_{VE,i}^*$.

Remark 7: The advantages of the two-stage minimization formulation are that (i) it streamlines the solution of the minimization problem in Eq. (3-6) to identify all the model parameters with improved accuracy and robustness; and (ii) it is computationally more efficient than the original problem in Eq. (3-6) in which all the model parameters must be identified simultaneously.

The validity of the proposed to estimate central aortic BP waveform from diametric PVR signals is shown in terms of the sample-by-sample RMSE as well as errors associated with SBP and PP. These errors are calculated between measured central aortic BP waveform and the same waveform estimated by the identified model from distal PVR signals (more specifically, using Eq. (3-22) and Eq. (3-25a) characterized by Θ^*).

To establish in-depth insight on the persistence of excitation properties associated with the proposed blind system identification approach, we examined the eigenvalues and eigenvectors of the data covariance matrix corresponding to Eq. (3-27). Using the time series sequences of $P_{Ci}(t)$, $i = 1{,}2$ and $1 \le t \le N$ where N is the length of the time series sequences, Eq. (3-27) can be rewritten into the following matrix equation:

$$\underbrace{\begin{bmatrix} P_{c1}(1+\tau_1+s_1+s_2+m_1+m_2) - P_{C2}(1+\tau_2+s_1+s_2+m_1+m_2) \\ \vdots \\ P_{c1}(N+\tau_1+s_1+s_2+m_1+m_2) - P_{C2}(N+\tau_2+s_1+s_2+m_1+m_2) \end{bmatrix}}_{\mathbf{Y}} \qquad (3\text{-}32)$$

$$= \underbrace{\begin{bmatrix} -\boldsymbol{\phi}_{\mathbf{0,1}}(1) & -\boldsymbol{\phi}_{\mathbf{1,1}}(1) & \boldsymbol{\phi}_{\mathbf{0},\mathbf{2}}(1) & \boldsymbol{\phi}_{\mathbf{1},\mathbf{2}}(1) \\ \vdots & \vdots & \vdots & \vdots \\ -\boldsymbol{\phi}_{\mathbf{0,1}}(N) & -\boldsymbol{\phi}_{\mathbf{1,1}}(N) & \boldsymbol{\phi}_{\mathbf{0},\mathbf{2}}(N) & \boldsymbol{\phi}_{\mathbf{1},\mathbf{2}}(N) \end{bmatrix}}_{\mathbf{\Phi}} \begin{bmatrix} \boldsymbol{h}_{\mathbf{11}} \\ \boldsymbol{h}_{\mathbf{12}} \\ \boldsymbol{h}_{\mathbf{21}} \\ \boldsymbol{h}_{\mathbf{22}} \end{bmatrix}$$

Noting that the solution to Eq. (3-32) is given by the least-squares technique as $(\mathbf{\Phi}^{\mathrm{T}}\mathbf{\Phi})^{-1}\mathbf{\Phi}\mathbf{Y}$, the eigenvalues and, eigenvectors of $\mathbf{\Phi}^{\mathrm{T}}\mathbf{\Phi}$ evaluated at the optimal PTTs τ_1^* and τ_2^* can be used to elucidate the model parameters persistently and poorly excited by the diametric PVR signals: the elements of the solution $[\boldsymbol{h}_{\mathbf{11}}^{\mathrm{T}} \quad \boldsymbol{h}_{\mathbf{12}}^{\mathrm{T}} \quad \boldsymbol{h}_{\mathbf{21}}^{\mathrm{T}} \quad \boldsymbol{h}_{\mathbf{22}}^{\mathrm{T}}]^{\mathrm{T}}$ associated with large eigenvalues are persistently excited and may thus be identified with accuracy, whereas those associated with small eigenvalues are poorly excited and may thus be identified with relatively poor accuracy.

3.6. Results and Discussion

We proposed a model-based blind system identification approach to estimate the central aortic BP waveform from a class of non-invasive diametric circulatory signals and demonstrated its feasibility by applying it to estimate central aortic BP waveform from two PVR signals measured at an upper arm and an upper leg for 10 subjects. Here, the validity of the mathematical model and the proposed blind system identification approach, as well as the accuracy of the central aortic BP estimated by the proposed approach is discussed. For our analysis, we consider the steady-state response of our dynamic model using stationary measured signals.

3.6.1. Model Structure Selection

Figure 3-3 shows a representative example of measured central aortic BP waveform and the same waveform estimated by the model in Eq. (3-23) using the parameters identified from standard input-output system identification when inputted with (a) arm and (b) leg distal PVR signals, while Table 3-1 summarizes the error metrics associated with all the subjects.

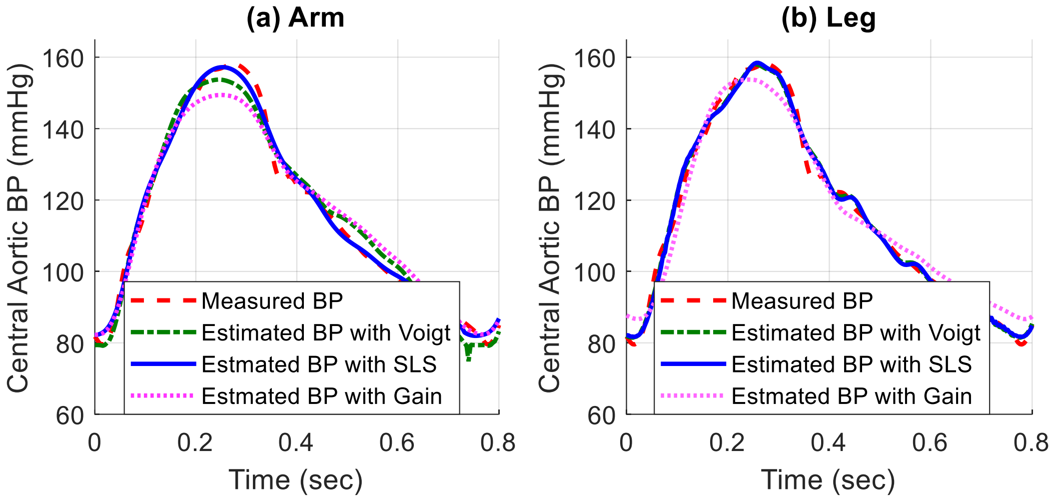

Figure 3-3- Representative example of measured central aortic BP waveform and the same waveform estimated by the model in Eq. (3-23) equipped with the parameters identified from standard input-output system identification when inputted with (a) arm and (b) leg distal PVR signals.

Overall, the proposed model structure is shown in Eq. (3-4) could reproduce the relationship between central aortic BP waveform and a non-invasive distal circulatory signal with accuracy. RMSEs, SBP errors and PP errors associated with the arm (with the SLS model) and leg (with the Voigt model) models were on average less than 2.0% and 1.4%, 2.5% and 3.5%, and 1.4% and 2.4% of the underlying MP, respectively.

Table 3-1- Error metrics obtained from model validation for central aortic BP waveforms estimated from the model in Eq. (3-23) for all subjects (mean±SD).

	Upper Arm			Leg		
	RMSE (mmHg)	SBP Error (mmHg)	PP Error (mmHg)	RMSE (mmHg)	SBP Error (mmHg)	PP Error (mmHg)
Gain Model	4.5±1.7	8.1±3.9	6.4±5.0	3.9±0.9	3.7±2.9	4.9±4.2
Voigt Model	4.5±2.1	2.6± 2.5	3.6±3.0	3.2± 1.7	1.3± 0.3	2.4±1.5
SLS Model	1.9± 0.7	1.2±0.4	2.2±0.9	2.7±1.5	1.4±0.6	2.4±2.1

In particular, it is shown that central aortic BP waveform was better estimated from the arm PVR signal with SLS model as the viscoelastic model (RMSE was significantly different between Voigt and SLS models and Gain and SLS models with $p<0.05$ (paired t-test)). While the same waveform was estimated well from the leg PVR signal when the Voigt model was used as the viscoelastic model, (RMSE was not significantly different between Voigt and SLS models). Interestingly, although the SLS model is a superset of the Voigt and Gain model, it did not always yield error metrics superior to the Voigt model due to the finite upper bounds we imposed on the parameter search space in the system identification procedure. Based on these results, we employed the SLS model as the viscoelastic model associated with the arm and the Voigt model as the viscoelastic model associated with the leg.

3.6.2. System Identification and Central Aortic BP Estimation

Figure 3-4 shows a representative example of (a) measured arm and leg PVR waveforms, (b) arm and leg BP waveforms estimated by the proposed blind system identification approach and Eq. (3-25a), and (c) measured central aortic BP waveform and the same waveform estimated by the proposed blind system identification approach and Eq. (3-26).

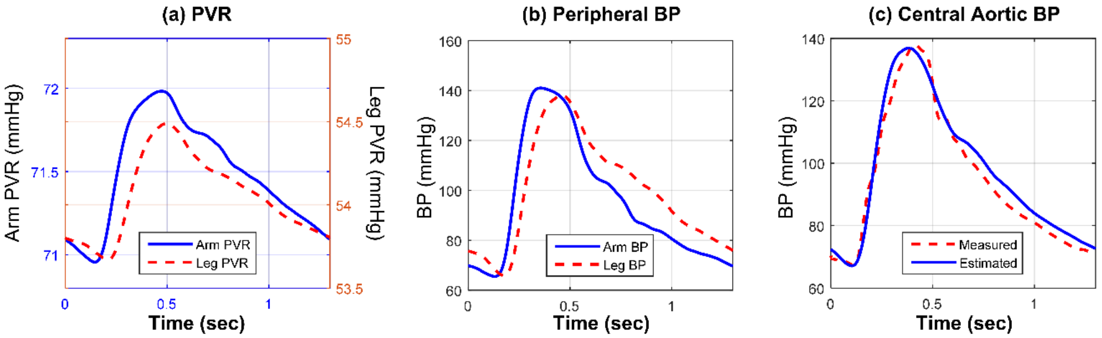

Figure 3-4- Representative example of (a) measured arm and leg PVR waveforms, (b) arm and leg BP waveforms estimated by the proposed blind system identification approach and Eq. (3-25a), and (c) measured central aortic BP waveform and the same waveform estimated by the proposed blind system identification approach and Eq. (3-26).

Overall, the proposed blind system identification approach could exploit two diametric PVR signals to estimate central aortic BP waveforms close to the measured central aortic BP waveforms in all 10 subjects. The error metrics (RMSE, SBP error, and PP error) calculated from the estimated central aortic BP waveforms were small: on average, the values are less than 4.5%, 2.5% and 2.1% of the underlying MP. Remarkably, these errors were largely smaller than the direct differences between central aortic BP and distal PVR waveforms (Table 3-2) which is mostly used in clinical practice currently. Noting that the inter-individual variability in the identified model parameters is quite large (see Table 3-2), which shows that the proposed approach may be able to deal with physiologic variability between different subjects and times in estimating central aortic BP waveform from diametric PVR signals.

Table 3-2- Model parameters and error metrics for central aortic BP waveforms estimated from the proposed blind system identification in Eq. (3-29)-(3-30) for all subjects (mean±SD).

(a) Model parameters.

	Tube-Load Model		
	τ (ms)	f_0	g_0
Arm	25±23	-0.43±0.34	0.04±0.03
Leg	78±30	0.08±0.79	0.33±0.41

	Viscoelastic Model		
	a_1 (mmHg)	a_0 (mmHg)	b_0
Arm	$6.30\times10^4\pm3.37\times10^4$	$-6.30\times10^4\pm3.37\times10^4$	$-1.00\pm7.78\times10^{-4}$
Leg	$2.11\times10^6\pm8.83\times10^5$	$-1.98\times10^6\pm8.80\times10^5$	1.0 ± 0.0

(b) Error metrics.

	RMSE (mmHg)	SBP Error (mmHg)	PP Error (mmHg)
Blind SYSID	4.43	3.20	3.63
Scaled Arm PVR	4.89	10.60	9.76
Scaled Leg PVR	6.27	8.31	12.34

From the analysis of the eigenvalues and eigenvectors associated with the data covariance matrix, it was found that the data covariance matrix exhibited a large condition number in all subjects (in the order of ~10^{23}) due to the sparse information contents in the distal PVR signals. This indicates that the matrix is numerically ill-conditioned and the solution $(\mathbf{\Phi}^{\mathrm{T}}\mathbf{\Phi})^{-1}\mathbf{\Phi}\mathbf{Y}$ to the matrix equation in Eq. (3-12) may suffer from inaccuracy due to numerical errors involved in the computation of the inverse matrix $(\mathbf{\Phi}^{\mathrm{T}}\mathbf{\Phi})^{-1}$. It is also noted that most eigenvectors associated with the small eigenvalues of $\mathbf{\Phi}^{\mathrm{T}}\mathbf{\Phi}$ closely align with the parameters in the viscoelastic models which could be a theoretical support that why the two-stage minimization with the exploitation of distal SP, MP and DP measurements is required to estimate the central aortic BP waveform more accurately, since SP, MP and DP measurements can play an important role in improving the quality of the identified viscoelastic models (see Eq. (3-29)).

In sum, the results presented support the feasibility of the proposed approach to the estimation of central aortic BP waveform from diametric PVR signals. Its applications to non-invasive circulatory signals other than PVR will be a meaningful next step.

3.6.3. Study Limitations

This study has a few limitations. First, we used estimates rather than measured distal SBP, MP and DBP values in validating the proposed approach. The estimated SBP, MP, and DBP were obtained from input-output system identification. Considering the accuracy of the mathematical models identified from the input-output system identification (see Figure 3-3 and Table 3-1), distal SBP, MP, and DBP estimated from the identified models are likely to be close to the (unknown) actual distal BP values. Yet, there can still be errors in the distal SBP, MP, and DBP we used. But more fundamentally, non-invasive auscultation and oscillometric BP measurements are known to incur errors with respect to invasive BP measurements [57]–[61]. Therefore, efforts to improve the accuracy of non-invasive BP measurement techniques (including auscultation and oscillometry) must accompany the efforts to estimate central aortic BP. As well, the impact of the errors involved in distal SP, MP and DP measurements on the accuracy of estimated central aortic BP waveform must be rigorously investigated. Finally, the feasibility of the proposed approach equipped with non-invasive distal SBP, MAP and DBP measurements must be experimentally evaluated.

Second, we did not validate the mathematical model in Eq. (3-23) on a component-by-component basis (that is, tube-load model and viscoelastic model separately). Such a model validation requires the measurements of invasive distal BP waveforms in addition to invasive central aortic BP waveform and distal PVR signals, which may not be trivial to obtain from human subjects due to ethical reasons. However, non-invasive techniques for BP waveform measurement are available, such as applanation tonometry [62]. Future work must consider incorporating viable measurements to enable a more comprehensive assessment of the proposed approach.

3.7. Conclusion

In this chapter, we developed a mathematical foundation to enable the estimation of central aortic BP waveform from non-invasive diametric circulatory signals, comprising the mathematical model, blind system identification procedure and parametric identifiability properties. Moreover, the feasibility of the proposed approach is validated with experimental data collected from human subjects.

Observer-Based De-Convolution of Deterministic Input in Coprime Multi-Channel Systems with Its Application to Non-Invasive Central Blood Pressure Monitoring

Chapter 4:

4.1. Introduction

More recently, attempts have been made to develop patient-specific techniques for estimating central aortic BP waveform from peripheral BP waveform measurements. The vast majority of these techniques are built upon the blind system identification methodology [79]. This methodology, when applied to coprime multi-channel systems with the unknown input signal, determines the channel dynamics and then de-convolves the input signal by exploiting the correlation relationship between the channels. In particular, the input-deconvolution step of the methodology has employed various techniques, such as direct inverse filtering [14], [45], least-squares and maximum-likelihood-type de-convolution [37], [46], and the design of dedicated de-convolution filters [35], [47].

In our endeavor to develop an input de-convolution technique equipped with robustness against the channel dynamics inaccuracy, we investigated the application of established state estimation techniques (i.e., the observers [80]) to input de-convolution in coprime multi-channel systems. The central idea underlying this technique is to derive the unknown input signal in a coprime multi-channel dynamical system by regarding it as a state variable to be estimated from multiple output signals from the system. This “closed-loop” input de-convolution idea was inspired by two key observations:

(i) A multi-channel system may be viewed as a hypothetical input-output system by designating its one output signal as input to the hypothetical input-output system and its another output signal as the output of the same system,

(ii) The observer may compensate for the adverse impact of the channel dynamics inaccuracy on the integrity of the de-convolved input signal by way of its corrective error feedback action.

In this chapter, we developed and analyzed an unknown input observer (UIO) for input de-convolution in coprime multi-channel systems, and illustrated its validity and potential using the clinically significant case study of estimating central aortic BP waveform from two non-invasively acquired peripheral arterial pulse waveforms.

4.2. Unknown Input Observer Design for Coprime Multi-Channel Linear Dynamical Systems

4.2.1. Problem Formulation

Consider a multi-channel linear dynamical system in which a common yet unknown input signal generates multiple output signals (Figure 5-1). It is assumed that the channels are coprime, i.e., they do not share common poles and/or zeros. The goal is to reconstruct the unknown input from the output signals at the multiple channels. The basic idea of the approach pursued in this work is to transform the multi-channel dynamics into an equivalent input-output dynamics in which the unknown input is cast into an internal state variable, and then to design an observer that can estimate the unknown input.

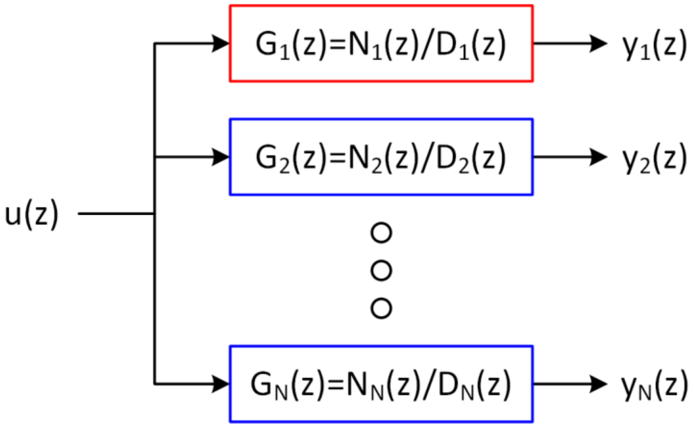

Figure 4-1- A coprime multi-channel linear dynamical system in which a common yet unknown input signal $u(z)$ generates multiple output signals $y_1(z)$ and $y_2(z)$.

4.2.2. Unknown Input Observer Design

Without loss of generality, the problem can be solved for a two-channel system case. Then, the results may be generalized and expanded to systems with more than two channels. Consider the following transfer functions for a two-channel system:

$$y_1(z) = G_1(z)u(z) = \frac{N_1(z)}{D_1(z)}u(z), y_2(z) = G_2(z)u(z) = \frac{N_2(z)}{D_2(z)}u(z) \tag{4-1}$$

where u is the common input, y_1 and y_2 are outputs, $G_1(z)$ and $G_2(z)$ are the channel transfer functions associated with y_1 and y_2, and $N_1(z)$, $D_1(z)$, $N_2(z)$, and $D_2(z)$ are polynomials in the discrete-time shift operator z of degrees m_1, n_1, m_2, and n_2, respectively. It is assumed that $D_1(z)$ and $D_2(z)$ are monic. It is further assumed that $m_1 = n_1$, i.e., $G_1(z)$ is a proper transfer function, and that $G_2(z)$ does not have any zeros at the origin. Note that the properness of $G_1(z)$ is not necessarily a restriction, because any strictly proper $G_1(z)$ can be made proper by padding z’s to its numerator polynomial $N_1(z)$: $\bar{N}_1(z) = z^{r_1}N_1(z)$, where $r_1 = n_1 - m_1$ is the relative degree of $G_1(z)$. In this way, an equivalent input-output relationship $\bar{y}_1(z) = \bar{G}_1(z)u(z) = \frac{\bar{N}_1(z)}{D_1(z)}u(z)$ with the forward-shifted output $\bar{y}(z) = y(z)z^{r_1}$ can be considered. The zeros at the origin in $G_2(z)$ can be handled similarly. Then, the unknown input $u(z)$ may be reconstructed from $y_1(z)$ and $y_2(z)$ as follows:

Theorem 2: Consider the two-channel system in Eq. (4-1) with $G_1(z)$ and $G_2(z)$ given by:

$$\begin{aligned}
G_1(z) &= \frac{N_1(z)}{D_1(z)} = \frac{b_{n_1}^{(1)} z^{n_1} + b_{n_1-1}^{(1)} z^{n_1-1} + \cdots + b_0^{(1)}}{z^{n_1} + a_{n_1-1}^{(1)} z^{n_1-1} + \cdots + a_0^{(1)}}, \\
G_2(z) &= \frac{N_2(z)}{D_2(z)} = \frac{b_{m_2}^{(2)} z^{m_2} + b_{m_2-1}^{(2)} z^{m_2-1} + \cdots + b_0^{(2)}}{z^{n_2} + a_{n_2-1}^{(2)} z^{n_2-1} + \cdots + a_0^{(2)}}
\end{aligned} \tag{4-2}$$

which satisfy the following properties:

1) The transfer functions $G_1(z)$ and $G_2(z)$ are coprime.
2) The polynomials $D_1(z)$ and $D_2(z)$ are monic.
3) The transfer function $G_1(z)$ is proper and minimum phase.
4) The transfer function $G_2(z)$ does not have any zero at the origin.

Let $\{A_1, B_1, C_1, D_1\}$ with $D_1 = b_{n_1}^{(1)}$ and $\{A_2, B_2, C_2, D_2\}$ with $D_2 = 0$ be the controllable canonical form realizations of $G_1(z)$ and $G_2(z)$, respectively. Then, the unknown input u of this coprime multi-channel system can be reconstructed by the following UIO:

$$\begin{aligned}
\hat{x}(k+1) &= \bar{A}\hat{x}(k) + \bar{B}y_1(k) + \bar{L}[y_2(k) - \bar{C}\hat{x}(k)], \\
\hat{u}(k) &= \frac{1}{b_{n_1}^{(1)}}\left[y_1(k) - \check{C}\hat{x}(k)\right]
\end{aligned} \tag{4-3}$$

where $x(k) = \begin{bmatrix} x_1(k) \\ x_2(k) \end{bmatrix}$ with x_1 and x_2 the state vectors of dimension n_1 and n_2, $\bar{A} = \begin{bmatrix} A_1 - B_1C_1/b_{n_1}^{(1)} & 0_{n_1 \times n_2} \\ -B_2C_1/b_{n_1}^{(1)} & A_2 \end{bmatrix}$, $\bar{B} = \frac{1}{b_{n_1}^{(1)}}\begin{bmatrix} B_1 \\ B_2 \end{bmatrix}$, $\bar{C} = [0_{1\times n_1} \quad C_2]$, $\check{C} = [C_1 \quad 0_{1\times n_2}]$, and $\bar{L}$

is a UIO gain matrix of dimension $(n_1 + n_2) \times 1$ with which all the eigenvalues of $\bar{A} - \bar{L}\bar{C}$ are placed in the unit circle.

Proof and Analysis: The state space realization of the multi-channel system in Eq. (4-1) is given by:

$$x(k+1) = \begin{bmatrix} A_1 & 0 \\ 0 & A_2 \end{bmatrix} x(k) + \begin{bmatrix} B_1 \\ B_2 \end{bmatrix} u(k),$$
$$\begin{bmatrix} y_1(k) \\ y_2(k) \end{bmatrix} = \begin{bmatrix} C_1 & 0 \\ 0 & C_2 \end{bmatrix} x(k) + \begin{bmatrix} b_{n_1}^{(1)} \\ 0 \end{bmatrix} u(k) \tag{4-4}$$

Given that, u is unknown but can be represented as a function of x_1 and y_1: $u(k) = \frac{1}{b_{n_1}^{(1)}}[y_1(k) - C_1x_1(k)]$, Eq. (4-4) can be rewritten as follows:

$$x(k+1) = \begin{bmatrix} A_1 & 0 \\ 0 & A_2 \end{bmatrix} x(k) + \begin{bmatrix} B_1 \\ B_2 \end{bmatrix} u(k)$$
$$= \begin{bmatrix} A_1 & 0 \\ 0 & A_2 \end{bmatrix} x(k) + \frac{1}{b_{n_1}^{(1)}} \begin{bmatrix} B_1 \\ B_2 \end{bmatrix} [y_1(k) - C_1x_1(k)] \tag{4-5}$$
$$= \bar{A}x(k) + \bar{B}y_1(k)$$
$$y_2(k) = C_2x_2(k) = \bar{C}x(k)$$

Hence, the UIO in Eq. (4-3) can reconstruct u from y_1 and y_2 if the pair $(\bar{A}, \bar{C})$ is observable. Noting that both $\{A_1, B_1, C_1, D_1\}$ and $\{A_2, B_2, C_2, D_2\}$ are associated with the controllable canonical form, we have:

$$A_1 = \begin{bmatrix} 0 & 1 & \\ \vdots & & \ddots \\ -a_0^{(1)} & \cdots & -a_{n_1-1}^{(1)} \end{bmatrix},$$
$$B_1 = \begin{bmatrix} 0 \\ \vdots \\ 1 \end{bmatrix}, \tag{4-6a}$$
$$C_1 = \begin{bmatrix} b_0^{(1)} - b_{n_1}^{(1)}a_0^{(1)} & \cdots & b_{n_1-1}^{(1)} - b_{n_1}^{(1)}a_{n_1-1}^{(1)} \end{bmatrix}$$

$$A_2 = \begin{bmatrix} 0 & 1 & \\ \vdots & & \ddots \\ -a_0^{(2)} & \cdots & -a_{n_2-1}^{(2)} \end{bmatrix},$$

$$B_2 = \begin{bmatrix} 0 \\ \vdots \\ 1 \end{bmatrix}, \tag{4-6b}$$

$$C_2 = \begin{bmatrix} b_0^{(2)} & \cdots & b_{m_2}^{(2)} & 0_{1\times(n_2-m_2)} \end{bmatrix}$$

Then, it can be easily shown that $\{A_3, B_3, C_3, D_3\} = \left\{A_1 - B_1C_1/b_{n_1}^{(1)}, B_1/b_{n_1}^{(1)}, -C_1/b_{n_1}^{(1)}, 1/D_1\right\}$ is the controllable canonical form realization of $G_1^{-1}(z)$. Indeed, using Eq. (4-6a):

$$A_1 - B_1C_1/b_{n_1}^{(1)} = \begin{bmatrix} 0 & 1 & \\ \vdots & & \ddots \\ -\frac{b_0^{(1)}}{b_{n_1}^{(1)}} & \cdots & -\frac{b_{n_1-1}^{(1)}}{b_{n_1}^{(1)}} \end{bmatrix} \triangleq A_3 \tag{4-7a}$$

$$-C_1/b_{n_1}^{(1)} = \begin{bmatrix} -\frac{b_0^{(1)}}{b_{n_1}^{(1)}} + a_0^{(1)} & \cdots & -\frac{b_{n_1-1}^{(1)}}{b_{n_1}^{(1)}} + a_{n_1-1}^{(1)} \end{bmatrix} \triangleq C_3 \tag{4-7b}$$

Eq. (4-7) yields $C_3(zI - A_3)^{-1}B_3 + D_3 = \frac{z^{n_1} + a_{n_1-1}^{(1)} z^{n_1-1} + \cdots + a_0^{(1)}}{b_{n_1}^{(1)} z^{n_1} + b_{n_1-1}^{(1)} z^{n_1-1} + \cdots + b_0^{(1)}} = G_1^{-1}(z)$.

Thus, $\bar{A}$ can be rewritten as $\bar{A} = \begin{bmatrix} A_3 & 0_{n_1\times n_2} \\ B_2C_3 & A_2 \end{bmatrix}$. Computing the observability matrix of the pair $(\bar{A}, \bar{C})$ yields:

$$\bar{O} = [O_1 \quad O_2] = \begin{bmatrix} 0_{r_2\times n_1} & C_2 \\ \vdots & C_2A_2 \\ \sum_{i=0}^{k-r_2-1} C_2A_2^{k-1-i}B_2C_3A_3^i & \vdots \\ \vdots & C_2A_2^{n_1+n_2-1} \end{bmatrix} \tag{4-8}$$

where $r_2 = n_2 - m_2$ is the relative degree of $G_2(z)$ and $r_2 + 1 \leq k \leq n_1 + n_2$. Since the pair (A_2, C_2) is observable, O_2 has full column rank, i.e., $\text{rank}(O_2) = n_2$. Further, O_1 reduces to the following after Gaussian elimination:

$$O_1 = \begin{bmatrix} 0_{r_2 \times n_1} \\ C_3 \\ C_3 A_3 \\ \vdots \\ C_3 A_3^{n_1+n_2-r_2-1} \end{bmatrix} \qquad (4\text{-}9)$$

which, since the pair (A_3, C_3) is observable and $n_1 + n_2 - r_2 - 1 \geq n_1$, guarantees that O_1 has full column rank, i.e., $\mathrm{rank}(O_1) = n_1$. Thus, $\bar{O}$ is a full rank matrix, meaning that the pair $(\bar{A}, \bar{C})$ is observable and the existence of the UIO in Eq. (4-3) is guaranteed.

Note that the rationale for the minimum phase requirement imposed on $G_1(z)$ is now obvious: according to Schur's determinant identity, the eigenvalues of $\bar{A}$ are given by those of A_2 and A_3:

$$\det(pI - \bar{A}) = \det(pI - A_2)\det(pI - A_3) \qquad (4\text{-}10)$$

In addition, the eigenvalues of A_3 correspond to the poles of $G_1^{-1}(z)$, i.e., the zeros of $G_1(z)$.

4.2.3. Intuitive Interpretation and Limiting Behavior

Intuitively, the UIO in Eq. (4-3) is equivalent to a Luenberger observer designed for the system with y_1 and y_2 as input and output and u as an internal state, i.e., $y_2(z) = G_2(z)G_1^{-1}(z)y_1(z)$ (Figure 4-2).

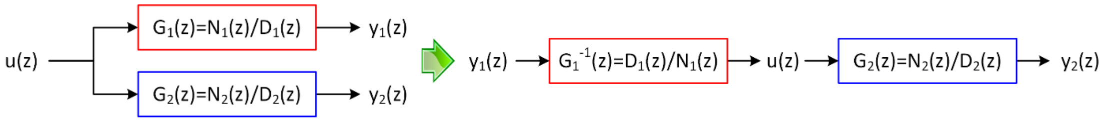

Figure 4-2- A hypothetical input-output system derived from a coprime multi-channel system by designating its one output signal as input to the hypothetical input-output system and its another output signal as the output of the same system.

Indeed, since $G_1(z)$ and $G_2(z)$ are coprime, a state space realization of the system is given by:

$$x_3(k+1) = A_3x_3(k) + B_3y_1(k),\ u(k) = C_3x_3(k) + D_3y_1(k) \tag{4-11a}$$

$$x_2(k+1) = A_2x_2(k) + B_2u(k),\ y_2(k) = C_2x_2(k) \tag{4-11b}$$

where $\{A_2, B_2, C_2, D_2\}$ and $\{A_3, B_3, C_3, D_3\}$ are the controllable canonical form realization of $G_2(z)$ and $G_1^{-1}(z)$ as defined in Eq. (4-6) and Eq. (4-7). Serially concatenating Eq. (4-11a) and Eq. (4-11b) yields:

$$\begin{bmatrix} x_3(k+1) \\ x_2(k+1) \end{bmatrix} = \begin{bmatrix} A_3 & 0_{n_1\times n_2} \\ B_2C_3 & A_2 \end{bmatrix} \begin{bmatrix} x_3(k) \\ x_2(k) \end{bmatrix} + \begin{bmatrix} B_3 \\ B_2/b_{n_1}^{(1)} \end{bmatrix} y_1(k) \tag{4-12a}$$

$$y_2(k) = \begin{bmatrix} 0_{1\times n_1} & C_2 \end{bmatrix} \begin{bmatrix} x_3(k) \\ x_2(k) \end{bmatrix} \tag{4-12b}$$

which is identical to Eq. (4-5). Thus, the UIO in Eq. (4-3) for the plant in Eq. (4-5) is identical to the Luenberger observer for the plant in Eq. (4-12).

The above intuitive insight streamlines the analysis of the limiting behavior of the UIO with respect to the magnitude of its gain $\bar{L}$. On the one hand, if $\bar{L} \approx 0$, Eq. (4-3) dictates that $\hat{u}(z) = G_1^{-1}(z)y_1(z)$; indeed, when $\bar{L} \approx 0$:

$$\begin{aligned} &\hat{x}_1(k+1) = A_3\hat{x}_1(k) + B_3y_1(k), \\ &\hat{u}(k) = \frac{1}{b_{n_1}^{(1)}}[y_1(k) - C_1\hat{x}_1(k)] = C_3\hat{x}_1(k) + D_3y_1(k) \end{aligned} \tag{4-13}$$

which is identical to Eq. (4-11a). Hence, $\hat{u}$ is essentially given by inverse filtering of $y_1(k)$ with $G_1(z)$. On the other hand, if $\bar{L} \to \infty$, Eq. (4-3) dictates that $\hat{u}(z) = G_2^{-1}(z)y_2(z)$; indeed, when $\bar{L}$ is very large:

$$\begin{aligned} \hat{x}_2(k+1) &= B_2C_3\hat{x}_1(k) + A_2\hat{x}_2(k) + \tfrac{B_2}{b_{n_1}^{(1)}}y_1(k) + L_2[y_2(k) - C_2\hat{x}_2(k)] \\ &= B_2C_3\hat{x}_1(k) + A_2\hat{x}_2(k) + \tfrac{B_2}{b_{n_1}^{(1)}}[C_1\hat{x}_1(k) + D_1\hat{u}(k)] + L_2[y_2(k) - C_2\hat{x}_2(k)] \\ &= B_2C_3\hat{x}_1(k) + A_2\hat{x}_2(k) + B_2[\hat{u}(k) - C_3\hat{x}_1(k)] + L_2[y_2(k) - C_2\hat{x}_2(k)] \\ &= A_2\hat{x}_2(k) + B_2\hat{u}(k) + L_2[y_2(k) - C_2\hat{x}_2(k)] \end{aligned} \tag{4-14}$$

In addition, very large $\bar{\mathrm{L}}$ enforces $\hat{\mathrm{y}}_2(\mathrm{k}) = \mathrm{C}_2\hat{\mathrm{x}}_2(\mathrm{k}) = \mathrm{y}_2(\mathrm{k})$, which, in conjunction with Eq. (4-14), yields:

$$\hat{\mathrm{x}}_2(\mathrm{k}+1) \cong \mathrm{A}_2\hat{\mathrm{x}}_2(\mathrm{k}) + \mathrm{B}_2\hat{\mathrm{u}}(\mathrm{k}), \hat{\mathrm{y}}_2(\mathrm{k}) = \mathrm{C}_2\hat{\mathrm{x}}_2(\mathrm{k}) \tag{4-15}$$

which reduces to $\hat{\mathrm{y}}_2(\mathrm{z}) \cong \mathrm{G}_2(\mathrm{z})\hat{\mathrm{u}}(\mathrm{z})$, i.e., $\hat{\mathrm{u}}$ is essentially given by inverse filtering of $\mathrm{y}_2(\mathrm{k})$ with $\mathrm{G}_2(\mathrm{z})$.

The above limiting behavior of the UIO provides an important insight into the fundamental limitation in its performance when applied to coprime multi-channel systems: the accuracy of the estimated unknown input approaches to that associated with the "open-loop" inverse filtering of y_1 with $\mathrm{G}_1(\mathrm{z})$ if the gain is chosen to be too small, whereas the accuracy approaches that associated with the "open-loop" inverse filtering of y_2 with $\mathrm{G}_2(\mathrm{z})$ if the gain is chosen to be too large. This unique limiting behavior can be attributed to the coprimeness of the channel dynamics as follows. The plant in Eq. (4-5) (or equivalently, Eq. (4-12); also see Figure 4-2) computes u from y_1 ($\mathrm{u}(\mathrm{z}) = \mathrm{G}_1^{-1}(\mathrm{z})\mathrm{y}_1(\mathrm{z})$), and then computes y_2 from u thus computed ($\mathrm{y}_2(\mathrm{z}) = \mathrm{G}_2(\mathrm{z})\mathrm{u}(\mathrm{z})$). Since the UIO reduces to the open-loop plant dynamics (i.e., Eq. (4-5)) when $\bar{\mathrm{L}} = 0$, and u can be estimated solely from y_1, $\hat{\mathrm{u}}(\mathrm{z}) = \mathrm{G}_1^{-1}(\mathrm{z})\mathrm{y}_1(\mathrm{z})$. On the other hand, when $\bar{\mathrm{L}} \to \infty$, the corrective error feedback acts to achieve $\tilde{\mathrm{y}}_2 \triangleq \mathrm{y}_2 - \hat{\mathrm{y}}_2 = 0$. In other words, u computed by the plant dynamics as $\mathrm{u}(\mathrm{z}) = \mathrm{G}_1^{-1}(\mathrm{z})\mathrm{y}_1(\mathrm{z})$ is corrected to yield $\hat{\mathrm{u}}$ to achieve $\mathrm{y}_2(\mathrm{z}) = \mathrm{G}_2(\mathrm{z})\, \hat{\mathrm{u}}(\mathrm{z})$. Thus, in this case, u can be estimated solely from y_2, $\hat{\mathrm{u}}(\mathrm{z}) = \mathrm{G}_2^{-1}(\mathrm{z})\mathrm{y}_2(\mathrm{z})$.

An important practical implication of the above limiting behavior associated with the UIO is that iterative trial and error process may be required to design a UIO whose performance is superior to simple open-loop inverse filtering. In contrast to conventional observer design problems (in which corrective error feedback action can be strengthened by simply increasing the observer gain, resulting in a larger difference between open-loop versus closed-loop state estimations), the gain of the UIO designed for coprime multi-channel systems must be carefully chosen (i.e., it must not be too small or not too large) to maximize the benefit of the corrective error feedback action.

4.3. Observer-Based De-Convolution of Central Aortic BP Waveform from Non-Invasive Peripheral Arterial Pulse Waveforms

To examine the validity, strengths, and limitations of the input de-convolution technique based on the UIO developed above, it was applied to a clinically significant real-world problem of estimating central aortic BP waveform from non-invasively acquired peripheral arterial pulse waveform measurements. The details of the problem formulation are provided in section 3.2. Specifically, PVR signals were made at the upper arm and leg sites using the BP cuffs loaded at a sub-diastolic pressure level. These diametric PVR signals were analyzed by a novel system identification procedure to derive the channel dynamics associated with (i) the propagation of the BP wave from the aorta to the peripheral arteries and (ii) the propagation of the peripheral BP waves to through the tissues to the BP cuffs to yield the PVR signals at the respective peripheral measurement sites. The focus of this work is to examine the validity of the input de-convolution technique based on the UIO by applying it to these BP wave propagation dynamics in the multi-channel arteries to estimate central aortic BP from peripheral PVR signals (Figure 4-3).

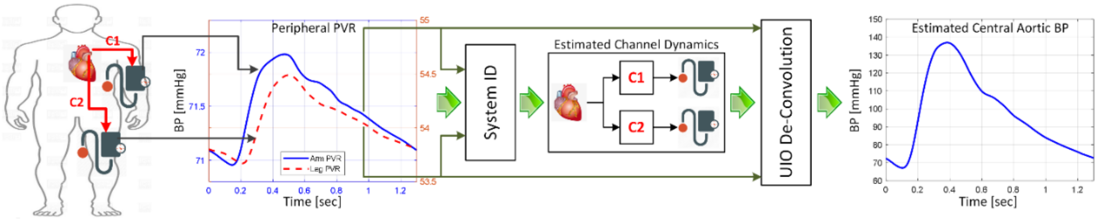

Figure 4-3- Observer-based de-convolution of central aortic blood pressure (BP) waveform from non-invasive peripheral arterial pulse waveform measurements.

4.3.1. Experimental Data

For evaluating this technique, the dataset described in 3.5.1 has been used. This experimental dataset contains central aortic BP and peripheral PVR signals from 10 cardiac catheterization patients at the University of Maryland Medical Center.

4.3.2. Plant Dynamics: Blood Pressure Wave Propagation in Multi-Channel Arteries

The plant dynamics considered in this work consists of two channels: one associated with the relationship between central aortic BP and arm PVR (C1; Figure 5-3), and the other associated with the relationship between central aortic BP and leg PVR (C2; Figure 4-3). Each channel dynamics is represented by (i) a tube-load model to represent the BP wave propagation in the artery, (ii) a viscoelastic model to represent the characteristics of the arterial wall and the tissues, and (iii) a physics-based model of the BP cuff as described in section 3.5 (Figure 3-1 and Eq. (3-17))

The physics-based BP cuff model involves nonlinearity, which is not suited to the UIO design developed in this work. However, these models can be inverted, i.e., the models allow for the computation of the peripheral BP waveforms from the corresponding PVR signals. Therefore, the UIO design was applied to the tube-load model component of the channel dynamics by considering the arm and leg BP waveforms (P_1& P_2) estimated from the corresponding PVR signals as the outputs of the channel dynamics expressed by Eq. (3-17).

4.3.3. UIO Design

For each patient, the UIO was designed in compliance with the assumptions of Theorem 2. First, the transfer function $G_i(z)$ associated with the channel Ci (Figure 4-3) was made proper by padding $2n_i$ forward shift operators z in its numerator polynomial (both $i = 1$ and $i = 2$ were considered). Second, the controllable canonical form realizations associated with the patient-specific channel dynamics $G_1(z)$ ($\{A_1, B_1, C_1, D_1\}$) and $G_2(z)$ ($\{A_2, B_2, C_2, D_2\}$) were obtained. Third, the matrices $\overline{A}$, $\overline{B}$, $\overline{C}$, and $\check{C}$ in Eq. (4-3) required for the UIO design were computed using the patient-specific controllable canonical form realizations thus obtained. Finally, the UIO in Eq. (4-3) was constructed by designing the gain $\overline{L}$.

Considering that the primary interest of this work was to investigate the validity and potential of the UIO-based input de-convolution technique, and also that the performance of the UIO approaches to open-loop inverse filtering if $\overline{L} = 0$ and $\overline{L} \to \infty$, the UIO gain $\overline{L}$ was designed by trial and error to investigate if any choice of $\overline{L}$ can lead to a UIO whose input de-convolution performance is superior to open-loop inverse filtering. Two approaches were specifically employed: pole placement and linear matrix inequality (LMI).

In the pole placement approach, the Butterworth pole layout [81] was considered as the desired pole locations for the closed-loop error dynamics in the continuous-time domain. For each patient, the continuous-time Butterworth poles with unspecified cut-off frequency were calculated according to the system order (i.e., the order of Eq. (4-3)). Then, a large number of candidate UIO pole locations were created by varying the cut-off frequency within its maximal value dictated by the sampling frequency $\mathrm{F_s}$ (i.e., $\frac{\pi}{\mathrm{F_s}}$). Subsequently, these candidate pole locations were transformed into the discrete-time domain. For each candidate pole location, a candidate UIO was designed with the pole placement technique [80]. The performance of the UIO was measured in terms of the RMSE between the true versus estimated central aortic BP waveforms. The UIO associated with the patient (called the UIO-PP hereafter) was then determined as the one exhibiting the smallest RMSE among all the candidate UIOs.

In the LMI approach, the UIO design problem was cast into an LMI problem as follows. Considering the following discrete-time Lyapunov function:

$$\mathrm{V}[\tilde{\mathrm{x}}(\mathrm{k})] = \tilde{\mathrm{x}}^{\mathrm{T}}(\mathrm{k})\mathrm{P}\tilde{\mathrm{x}}(\mathrm{k}) > 0, \mathrm{P} > 0 \tag{4-16}$$

The UIO must satisfy the following asymptotic stability condition:

$$\mathrm{V}[\tilde{\mathrm{x}}(\mathrm{k}+1)] - \mathrm{V}[\tilde{\mathrm{x}}(\mathrm{k})] < 0 \tag{4-17}$$

Based on the UIO in Eq. (4-3), the error dynamics are given by:

$$\tilde{\mathrm{x}}(\mathrm{k}+1) = (\bar{\mathrm{A}} - \bar{\mathrm{L}}\bar{\mathrm{C}})\tilde{\mathrm{x}}(\mathrm{k}) \tag{4-18}$$

Hence, Eq. (4-17) is satisfied if and only if the following inequality is satisfied:

$$(\bar{\mathrm{A}} - \bar{\mathrm{L}}\bar{\mathrm{C}})^{\mathrm{T}}\mathrm{P}(\bar{\mathrm{A}} - \bar{\mathrm{L}}\bar{\mathrm{C}}) - \mathrm{P} < 0 \tag{4-19}$$

Using the Schur complement and the change of variable $\mathrm{K} = \bar{\mathrm{L}}^{\mathrm{T}}\mathrm{P}$, Eq. (4-19) can be cast into the following LMI:

$$\begin{bmatrix} -\mathrm{P} & (\bar{\mathrm{A}}^{\mathrm{T}}\mathrm{P} - \bar{\mathrm{C}}^{\mathrm{T}}\mathrm{K}) \\ (\bar{\mathrm{A}}^{\mathrm{T}}\mathrm{P} - \bar{\mathrm{C}}^{\mathrm{T}}\mathrm{K})^{\mathrm{T}} & -\mathrm{P} \end{bmatrix} < 0 \tag{4-20}$$

Once the matrix K satisfying Eq. (4-20) is found, the UIO gain $\bar{\mathrm{L}}$ can be determined by $\bar{\mathrm{L}} = \mathrm{P}^{-1}\mathrm{K}^{\mathrm{T}}$.

For each patient, the UIO was designed by solving the LMI feasibility problem in Eq. (4-20) with a constraint on the desired pole locations to optimize the error convergence rate: $|z| < \sigma$ (by which the settling time of the UIO error convergence has a settling time smaller than $\frac{4}{F_s \ln \sigma}$). Specifically, Eq. (4-20) was solved while varying the value of σ in the range of (0, 1) and selecting the one that yield a large number of candidate UIOs. Similar to the pole placement technique above, the performance of the UIO was measured in terms of the RMSE between the true versus estimated central aortic BP waveforms. The UIO associated with the patient (called the UIO-LMI) was then determined as the one exhibiting the smallest RMSE among all the candidate UIOs.

4.3.4. UIO Performance Analysis

The performance of UIO-PP and UIO-LMI was measured in terms of the waveform RMSE as well as the absolute errors associated with systolic (SBP error) and pulse (PP error = systolic – diastolic) pressures between the true versus estimated central aortic BP waveforms. These errors were computed for each patient. Then, the mean and SD were calculated.

To assess the performance of the UIO in estimating central aortic BP waveform relative to the conventional as well as primitive techniques, the same error metrics (RMSE, SBP error, and PP error) were also computed for the conventional open-loop inverse filtering technique as well as the arm and leg PVR signals scaled to central aortic diastolic and mean pressures. For each patient, the open-loop inverse filtering technique was performed by filtering (i) the arm PVR signal by the inverse of $G_1(z)$ as well as (ii) the leg PVR signal by the inverse of $G_2(z)$ to yield the estimated central aortic BP waveforms. For each patient, PVR scaling was performed by linearly calibrating the arm and leg PVR signals so that the diastolic and mean pressure levels associated with the PVR signals become identical to the central aortic diastolic and mean pressures measured from the patient. Then, the aforementioned error metrics between the true central aortic BP waveform versus these waveforms were computed for each patient, whose mean and SD were subsequently calculated.

Statistical significance in the difference between the error metrics associated with UIO, open-loop inverse filtering, and scaled PVR signals was determined with the Wilcoxon signed-rank test, where the Bonferroni correction factor of 2 was used to account for the multiple comparisons (i.e., UIO-PP versus inverse filtering and scaled PVR signals, as well as UIO-LMI versus inverse filtering and scaled PVR signals).

4.4. Results and Discussion

Table 4-1 summarizes RMSE, SPE, and PPE associated with central aortic blood pressure waveforms derived from UIO-PP, UIO-LMI, open-loop inverse filtering, and scaled PVR signals, while Figure 4-4 illustrates a few representative examples of true versus estimated central BP waveforms: (a) an example where UIO shows performance marginally superior to inverse filtering and (b) an example where UIO shows performance largely superior to inverse filtering.

Table 4-1- The root-mean-squared errors (RMSEs), systolic blood pressure errors (SP errors), and pulse pressure errors (PP errors) associated with central aortic blood pressure waveforms derived from UIO-PP, UIO-LMI, open-loop inverse filtering (IF), and scaled PVR signals (N=10). UIO-PP: UIO designed with pole placement. UIO-LMI: UIO designed with LMI.

(a) UIO-PP

	UIO-PP$_1$ ($y_1 = P_1$)	UIO-PP$_2$ ($y_1 = P_2$)	Average
RMSE [mmHg]	3.7+/-1.7	3.6+/-1.0	3.7+/-1.4[*†]
SBP error [mmHg]	2.7+/-2.0	2.4+/-1.6	2.6+/-1.7[†]
PP error [mmHg]	3.2+/-3.4	2.9+/-1.9	3.0+/-2.7[*†]

[*]: p<0.025 with respect to inverse filtering (Wilcoxon signed-rank test).
[†]: p<0.025 with respect to scaled PVR signals (Wilcoxon signed-rank test).

(b) UIO-LMI

	UIO-LMI$_1$ ($y_1 = P_1$)	UIO-LMI$_2$ ($y_1 = P_2$)	Average
RMSE [mmHg]	4.2+/-2.0	4.4+/-1.7	4.3+/-1.8[*]
SBP error [mmHg]	3.4+/-3.1	3.3+/-2.0	3.3+/-2.6[†]
PP error [mmHg]	4.8+/-4.1	4.9+/-3.4	4.8+/-3.7

[*]: p<0.025 with respect to inverse filtering (Wilcoxon signed-rank test).

[†]: p<0.025 with respect to scaled PVR signals (Wilcoxon signed-rank test).

(c) Inverse Filtering

	IF$_1$ ($y_1 = P_1$)	IF$_2$ ($y_1 = P_2$)	Average
RMSE [mmHg]	5.3+/-2.4	4.9+/-1.9	5.1+/-2.1
SBP error [mmHg]	5.5+/-4.7	2.8+/-2.2	4.2+/-3.9
PP error [mmHg]	7.2+/-5.1	3.9+/-4.3	5.5+/-4.9

(d) Scaled PVR Signals

	Arm PVR	Leg PVR	Average
RMSE [mmHg]	4.6+/-1.8	5.8+/-2.6	5.2+/-2.3
SBP error [mmHg]	8.8+/-6.2	6.2+/-5.8	7.5+/-6.0
PP error [mmHg]	7.7+/-6.3	8.8+/-9.2	8.2+/-7.7

The input de-convolution based on the UIO was in general superior to open loop inverse filtering (which represents the limiting performance of the UIO at $\bar{L} = 0$ and $\bar{L} \to \infty$), suggesting that the corrective error feedback action provided by the UIO is practically meaningful. On average, the RMSE associated with the UIO-PP was 27.5% smaller than the open-loop inverse filtering and 28.8% smaller than the scaled arm and leg PVR signals (Table 4-1). Likewise, the RMSE associated with the UIO-LMI was 15.7% smaller than the open-loop inverse filtering and 17.3% smaller than the scaled arm and leg PVR signals (Table 4-1). In the case of UIO-PP, the UIO designed with P_1 and P_2 designated as its input and output (i.e., $y_1 = P_1$ and $y_2 = P_2$ in Eq. (4-3); UIO-PP$_1$ in Table 4-1) was superior to the open-loop inverse filtering based on both P_1 (i.e., $\bar{L} = 0$; IF$_1$ in Table 4-1) and P_2 (i.e., $\bar{L} \to \infty$; IF$_2$ in Table 4-1) in all 10 patients, while the UIO designed with P_2 and P_1 designated as its input and output (i.e., $y_1 = P_2$ and $y_2 = P_1$ in Eq. (4-3); UIO-PP$_2$ in Table 4-1) was superior to the same open-loop inverse filtering (i.e., IF$_1$ and IF$_2$) in most (i.e., 8) patients. In the case of UIO-LMI, the UIO designed with (i) P_1 and P_2 designated as its input and output (UIO-LIM$_1$ in Table 4-1) and (ii) P_2 and P_1 designated as its input and output (UIO-LMI$_2$ in Table 4-1) was superior to both IF$_1$ and IF$_2$ in 6 and 5 patients, respectively. In the remaining patients whose UIO did not excel both IF$_1$ and IF$_2$, the UIO exhibited an RMSE value between the RMSE values associated with IF$_1$ and IF$_2$, as predicted by the mathematical analysis presented in Section 4.2.3. Both UIO-PP and UIO-LMI exhibited RMSE values smaller than those associated with the scaled arm and leg PVR signals in 7 and all 10 patients, respectively.

The input de-convolution based on UIO-PP also estimated central aortic blood pressure waveform whose SPE and PPE are smaller than those associated with both open-loop inverse filtering and scaled PVR signals. On the average, the SPE and PPE associated with the UIO-PP were 38.1% and 45.5% smaller than open-loop inverse filtering, and 56.3% and 63.4% smaller than the scaled arm and leg PVR signals (Table 4-1). The SPE and PPE associated with the UIO-LMI were likewise 21.4% and 12.7% smaller than open-loop inverse filtering, and 56.0% and 41.5% smaller than the scaled arm and leg PVR signals (Table 4-1). This is notable in that SPE and PPE were not explicitly optimized during the UIO design process (although they may improve as the waveform accuracy is optimized). However, in contrast to UIO-PP (which yielded average SPE and PPE values smaller than the same values associated with both IF$_1$ and IF$_2$), UIO-LMI yielded average SPE and PPE values between the same values associated with IF$_1$ and IF$_2$ (except for UIO-LMI$_2$, whose average SPE was smaller than those associated with both IF$_1$ and IF$_2$; Table 4-1).

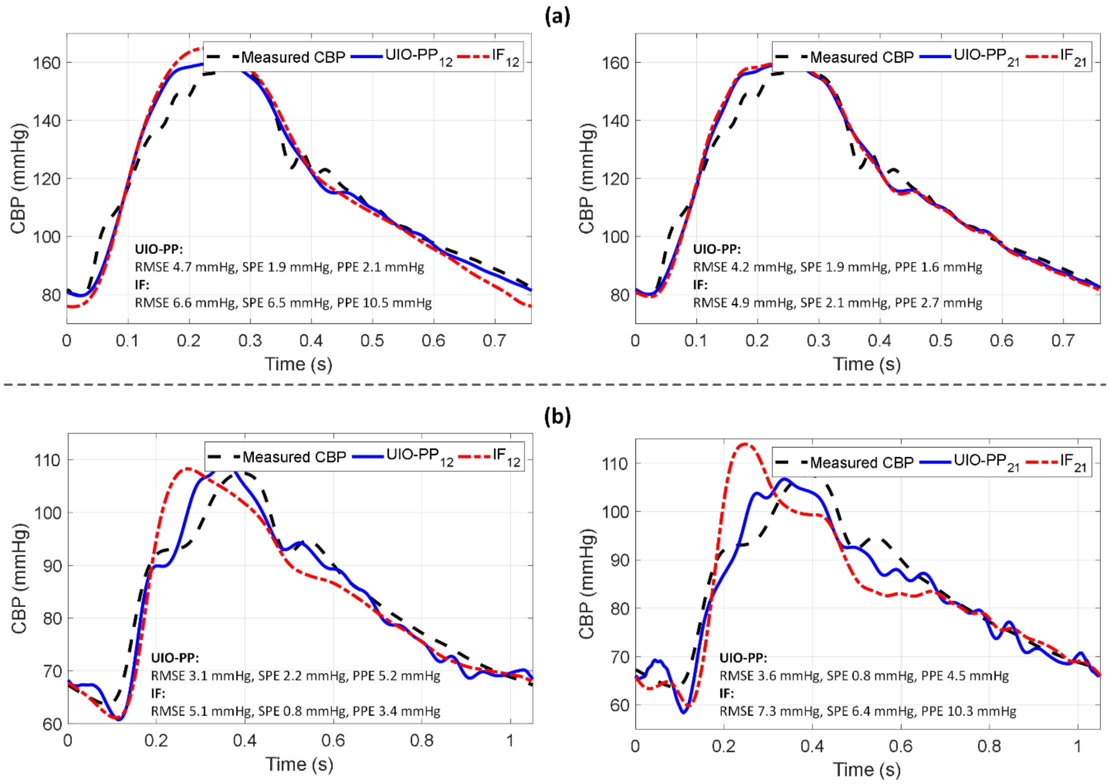

Figure 4-4- Representative examples of true versus estimated central BP waveforms: (a) an example where UIO-PP shows performance marginally superior to inverse filtering and (b) an example where UIO-PP shows performance largely superior to inverse filtering.

Comparing UIO-PP and UIO-LMI, the UIO-PP yielded superior accuracy than UIO-LMI. However, its design process was more ad-hoc and resource-intensive. In fact, the UIO-PP was obtained by rigorously optimizing the RMSE metric associated with the central aortic blood pressure waveform, whereas the UIO-LMI was obtained simply by solving an LMI feasibility problem with a rudimentary constraint. It is plausible that the efficacy of the UIO-LMI may further be improved by augmenting the currently used LMI problem formulation with more stringent constraints that specify the transient and steady-state behaviors of the error convergence dynamics. Similarly, the efficacy of the UIO-PP may likewise be improved by considering a wide range of desired closed-loop pole locations. But in any case, given that the performance of the UIO-based input de-convolution technique is bounded by the open-loop inverse filtering, both design procedures may require careful selection and tuning of the observer gain.

4.5. Conclusions

In our attempt to enable accurate patient-specific estimation of central aortic blood pressure waveform from non-invasively acquired peripheral arterial pulse waveforms, we developed and validated an observer-based closed-loop approach to input de-convolution in coprime multi-channel linear dynamical systems. A universal design algorithm for a UIO was presented with an insightful mathematical analysis to elucidate its physical implications and inherent performance limitations. The results obtained from the experimental data showed promise and consistency with the mathematical analysis.

Estimation of Cardiovascular Risk Predictors from Non-Invasively Measured Diametric Pulse Volume Waveforms via Multiple Measurement Information Fusion

Chapter 5:

5.1. Introduction

There are some efforts to enable more convenient and affordable estimation and tracking of CV risk predictors based on the automated cuff devices [63]–[70]. In this approach, the PVR waveform of the brachial artery is measured while the cuff pressure is maintained at a constant sub-diastolic or supra-systolic level. The PVR waveform is then calibrated to the arm cuff BP measurement and converted to central BP waveform using a mathematical transformation. However, as discussed earlier, most of the prior methods suffer from two deficiencies which may affect the results:

(1) the techniques rely on population-based transformation (GTF) to formulate the relation between the arm PVR waveform and central BP waveform and thus may not achieve optimal accuracy.

(2) CV risk predictors other than central BP, especially those associated with the central aorta (such as aortic PP amplification and PWV), cannot be readily estimated in the absence of distal aortic pulse measurement.

In prior work, it has been demonstrated that CV risk predictors including central BP [14], [35]–[37], PTT [71], and wave reflection characteristics [72] may be estimated in subject-specific fashion from arterial pulse waveforms measured at the body's diametric locations. However, so far, this multiple measurement approach has been validated with invasive diametric BP waveforms. Yet, considering already available dual-cuff devices [67], [73]–[75], this approach has potential to be integrated with such devices to yield convenient, affordable, and subject-individualized CV risk predictors estimation and tracking technologies.

In this chapter, we present a novel multiple measurement information fusion approach to the estimation of CV risk predictors from non-invasive circularity PVR waveforms measured at the body's diametric locations. In this approach, CV risk predictors are estimated in three steps by:

(1) Deriving lumped-parameter models of the central-diametric arterial lines from circularity PVR waveforms,

(2) Using the mathematical arterial model to estimate the central BP waveform by analyzing the diametric PVR waveforms,

(3) Estimating CV risk predictors (including central SBP and PP, PP amplification, and PTT) from the arterial line models and central BP waveform.

5.2. CV Risk Predictors Estimation from Diametric PVR via Multiple Measurement Information Fusion

5.2.1. Experimental Protocol

We studied electronically archived data from 164 human subjects that were originally obtained in a previous study under IRB approval and written informed consent [53]. These subjects had central BP waveform measured at the carotid artery using the applanation tonometry, as well as PVR waveform recordings from the upper arm (i.e., brachial artery) and ankle (i.e., posterior-tibial artery) using automated arm and ankle cuff devices. The carotid BP and PVR waveforms were calibrated using the brachial MAP and DP obtained using the oscillometric BP measurement method. We randomly split the 164 subjects into 50 for training and 114 for testing.

This data set compared to the one used in the previous chapters and explain in section 3.5.1 has some differences which will be important during this study. First, in this data, the carotid BP is measured non-invasively. However numerous studies reported that this non-invasive BP waveform can be considered as a surrogate of invasive aortic BP waveform [17], [76]. Second, the second PVR signal is measured from ankle though previous data set contains PVR measurements from the upper leg. And third, the PVR signals were calibrated by measured BP values in distal locations. All these differences bring to modify the model introduced in section 3.5.2 which will be explained in section 5.2.2.

From the data, the following reference CV risk predictors were computed. First, reference central SBP and PP were computed as the carotid SBP and PP. Second, reference aortic PP amplification was computed as the ratio of carotid PP and ankle PP. Third, reference aortic PTT was computed as the time delay between the diastolic troughs of the carotid BP and ankle PVR waveforms [77].

5.2.2. Mathematical Modeling and Model Structure Selection

The proposed multiple measurements information fusion approach estimates CV risk predictors from diametric PVR waveforms in three steps. Step 1: A lumped-parameter models of the central-diametric arterial lines are derived from diametric pulse volume (PVR) waveforms using Eq. (2-3). Step 2: Central blood pressure (BP) waveform is estimated by analyzing the diametric PVR waveforms using the derived arterial line models using Eq. (5-2). Step 3: CV risk predictors (including central BP waveform, central systolic and pulse pressures, pulse pressure amplification, and pulse transit time) are estimated from the arterial line models and central BP waveform in conjunction with the diametric PVR waveforms.

The lumped-parameter central-diametric arterial line models are derived from diametric PVR waveforms by using the same concept as before those diametric PVR waveforms originate from the common central pulse waveform from the heart. Our previous results show that occlusive cuffs behavior can be modeled linearly in the blood pressure range. Therefore, a simpler model than the model introduced in section 3.2. is used for this dataset. The model structure selection for the viscoelastic model will be also slightly different since the second measured PVR signal is from the ankle. This model was developed and validated by Lee et al. [78].

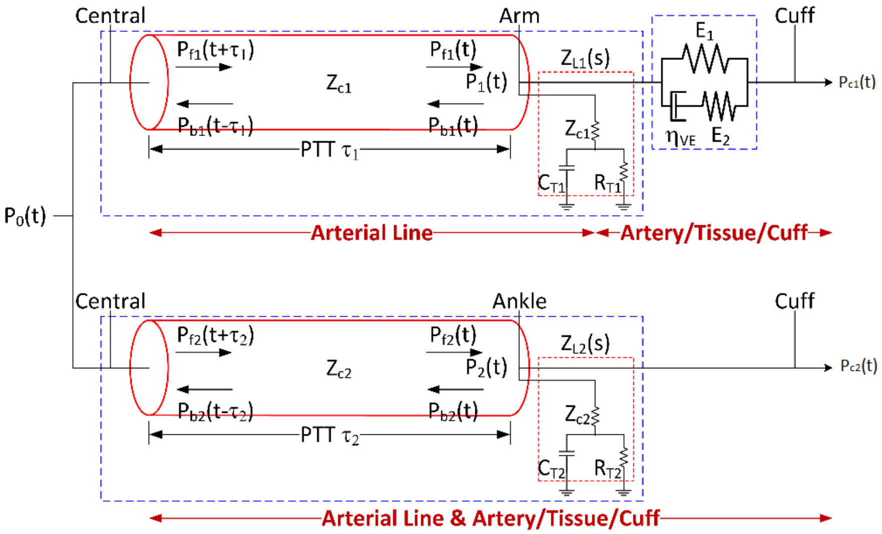

Figure 5-1- Lumped-parameter (tube-load) models to relate central blood pressure (BP) waveform to diametric pulse volume (PVR) waveform.

So, the relation between central BP waveform (P_0) to the arm (P_{C1}) and ankle (P_{C2}) PVR waveforms (Figure 5-1) can be formulated as:

$$
\begin{aligned}
P_{C1}(s) &= G_1(s)P_0(s) = \frac{E_2+\eta_{VE}s}{E_1E_2+(E_1+E_2)\eta_{VE}s}\frac{s+\eta_{11}+\eta_{21}}{e^{\tau_1 s}(s+\eta_{11})+e^{-\tau_1 s}\eta_{21}}P_0(s) \\
P_{C2}(s) &= G_2(s)P_0(s) = \frac{s+\eta_{12}+\eta_{22}}{e^{\tau_2 s}(s+\eta_{12})+e^{-\tau_2 s}\eta_{22}}P_0(s)
\end{aligned}
\tag{5-1}
$$

where s is the Laplace operator, τ_1 and τ_2 are the central-arm and central-ankle PTTs, respectively, η_{ij}, $j = 1{,}2$ are the polynomial parameters associated with the $P_{Cj}(s)$, while E_1, E_2, and η_{VE} are the parameters characterizing the viscoelastic model associated with the brachial artery-tissue-arm cuff interface. To apply the MBSI using Eq. (2-3), Eq. (2-4) could be rewrite as below:

$$
\begin{aligned}
\theta^* = \arg\min_{\theta}\{&\left\|\mathcal{L}^{-1}[G_1^{-1}(s,\theta)P_{C1}(s) - G_2^{-1}(s,\theta)P_{C2}(s)]\right\| \\
&+ \left\|\max(\mathcal{L}^{-1}[G_1^{-1}(s,\theta)P_{C1}(s)]) - \max(\mathcal{L}^{-1}[G_2^{-1}(s,\theta)P_{C2}(s)])\right\| \\
&+ \left\|(\max(\mathcal{L}^{-1}[G_1^{-1}(s,\theta)P_{C1}(s)]) \right. \\
&- \min(\mathcal{L}^{-1}[G_1^{-1}(s,\theta)P_{C1}(s)])) \\
&- (\max(\mathcal{L}^{-1}[G_2^{-1}(s,\theta)P_{C2}(s)]) \\
&\left. - \min(\mathcal{L}^{-1}[G_2^{-1}(s,\theta)P_{C2}(s)]))\right\|\}
\end{aligned}
\tag{5-2}
$$

where $\mathcal{L}$ is the Laplace transform operator and $\theta = \{\tau_1, \tau_2, \eta_{11}, \eta_{21}, \eta_{12}, \eta_{22}, E_1, E_2, \eta_{VE}\}$ is the vector of unknown arterial line model parameters. Since Eq. (5-2) is solved using P_{C1} and P_{C2} measured from a specific subject, θ^* derived from Eq. (5-2) is specific to the subject at the time of the PVR measurement. It must be noted that the multiple measurement information fusion approach requires $G_1(s)$ and $G_2(s)$ to be distinct in Eq. (2-3) to be non-trivial. Considering that arterial line dynamics associated with diametric locations are expected to be highly distinct from each other, it is preferable to employ diametric PVR waveforms in realizing the multiple measurement information fusion approach.

The central BP waveform specific to the subject can be estimated from P_{C1} and P_{C2} and the subject-specific arterial line models as follows:

$$\hat{P}_0(s) = \sigma_1\hat{P}_{01}(s) + \sigma_2\hat{P}_{02}(s) = \sigma_1 G_1^{-1}(s,\theta^*)P_{C1}(s) + \sigma_2 G_2^{-1}(s,\theta^*)P_{C2}(s) \tag{5-3}$$

where $\hat{P}_0(s)$ denotes the estimated central BP waveform, $\hat{P}_{01}(s) = G_1^{-1}(s,\theta^*)P_{C1}(s)$ and $\hat{P}_{02}(s) = G_2^{-1}(s,\theta^*)P_{C2}(s)$ are the central BP waveforms estimated from P_{C1} and P_{C2}, respectively, and $0 \leq \sigma_1, \sigma_2 \leq 1$ are the weights (note that $\sigma_1 + \sigma_2 = 1$). As before, for this problem we assumed $\sigma_1 = \sigma_2 = 0.5$.

The CV risk predictors can then be estimated as follows. Central SBP and PP can be estimated as the maximum and amplitude values associated with $\hat{P}_0$. Aortic PP amplification can be estimated as the ratio of estimated central PP and the amplitude value associated with the ankle PVR waveform. Aortic PTT can be estimated as τ_2^* obtained from Eq. (5-2).

5.2.3. Data Analysis

In this study, the performance of the multiple measurement information fusion approach to the estimation of CV risk predictors from non-invasive diametric PVR waveforms in comparison with the state-of-the-art population-based GTF approach has been studied.

A set of GTFs associated with the carotid BP and diametric PVR waveform measurements are considered: an arm GTF based on the tube-load model with a SLS model (taking the form of $G_1(s)$ in Eq. (5-1) with population-averaged parameters, called hereafter the arm TLS GTF), an arm GTF based on the tube-load model with a static gain (taking the form of $G_1(s)$ in Eq. (5-1) with $\eta_{VE} = 0$ and population-averaged parameters, called hereafter the arm TLG GTF), and an ankle GTF based on the tube-load model (taking the form of $G_2(s)$ in Eq. (5-1) with population-averaged parameters, called hereafter the ankle TL GTF). Each GTF was constructed by first deriving the corresponding arterial line model parameters associated with each of the 50 subjects in the training data from the subject's carotid BP and PVR waveforms via numerical optimization (similar to Lee et al. work [78]), and then implementing the same arterial line model characterized by the median values of the model parameters derived for that 50 subjects. We compared these GTFs in terms of their accuracy in estimating central BP waveform from the respective PVR waveforms, including the RMSE waveform error, absolute SBP and PP errors (e_{SP} and e_{PP}), and SBP and PP error norm ($= \sqrt{e_{SP}^2 + e_{PP}^2}$) across the 50 subjects. The best-performing GTF is used as the reference technique in investigating the performance of the multiple measurement information fusion approach in the blind testing stage.

Also, a set of realizations of the multiple measurement information fusion approach (ITFs) was studied as well. First, the fully individualized transfer function is optimized as described in section 5.2. (f-ITF), in which all the elements in θ in Eq. (5-2) are individualized using the training data, so its accuracy in estimating central BP waveform from diametric PVR waveforms (including the RMSE, absolute SBP and PP errors, and SBP and PP error norm) was minimized across the 50 subjects in the training data. Second, two partially individualized transfer functions are constructed (p-ITFs, in that only a subset of the elements in θ in Eq. (5-2) are individualized based on the optimized f-ITF). The idea behind these models is to create individualized transfer functions equipped with improved performance and robustness by relaxing the complexity of the optimization problem in Eq. (5-2), thereby avoiding high-variance model parameters as well as overfitting. One was constructed by fixing the model parameter(s) which exhibited the smallest inter-individual variability across the 50 subjects in the training data (called hereafter the p-ITF$_1$), while the other was constructed by fixing the polynomial parameters η_{11} and η_{21} in $G_1(s)$, which are known to often have little impact on the transfer function and may thus be fixed at appropriate nominal values [14], [35]. These p-ITFs are derived by solving Eq. (5-2) with respect to the set of parameters to be individualized while fixing the remaining parameter(s) to nominal value(s). These ITFs are compared in terms of their accuracy in estimating central BP waveform from diametric PVR waveforms. Then, the best-performing ITF(s) in the blind testing stage is studied.

A blind testing is utilized to investigate the performance of the best-performing GTF and ITFs as follows. First, the best-performing GTF and ITFs are compared in terms of their accuracy in estimating central BP waveform. Second, the relevance of the CV risk predictors estimated from the ITFs are judged in terms of their correlations with the reference CV risk predictors obtained directly from the carotid BP and ankle PVR waveform measurements. Third, the performance of the ITFs relative to the GTF is inspected with respect to different degrees of PP amplification.

5.2.4. Statistical Analysis

The paired t-test is used in comparing the (1) arm TLS, arm TLG, and ankle TL GTFs; (2) f-ITF, p-ITF$_1$, and p-ITF$_2$; and (3) best-performing GTF and ITFs. A significance level of p=0.05 is considered with the Holm-Bonferroni correction to counteract the influence of multiple comparisons.

5.3. Results & Discussion

In this section, the results of the proposed multiple measurement information fusion approach to the estimation of CV risk predictors from non-invasive diametric PVR waveforms are presented.

5.3.1. Experimental Data

Table 5-1 shows the demographic information of the subjects analyzed in this study (median (IQR)). CV risk predictors, including BP (MP: 56-159 mmHg; DP: 44-131 mmHg), carotid-ankle PP amplification (1.01-1.55), and PTT (carotid-arm: 24-124 ms; carotid-ankle: 80-200 ms) varied widely in these subjects, indicating that the data are diversely distributed to rigorously examine the validity and performance of the GTFs and ITFs under a wide range of physiological states.

Table 5-1- Subject demographics (median (IQR)).

	Training Data (N=50)	Testing Data (N=114)	All Data (N=164)
Age (Years)	58 (46 - 70)	56 (45 - 69)	57 (45 - 69)
Gender	M 29 / F 21	M 60 / F 54	M 89 / F 75
Height (cm)	165 (160 - 168)	160 (153 - 167)	162 (155 - 167)
Weight (kg)	63 (59 - 72)	60 (52 - 68)	61 (53 - 69)
Mean BP (mmHg)	90 (82 - 108)	93 (81 - 105)	93 (81 - 106)
Diastolic BP (mmHg)	73 (66 - 86)	76 (65 - 83)	76 (65 - 84)
Carotid-Ankle PP Amplification	1.12 (1.06 - 1.21)	1.17 (1.08 - 1.28)	1.15 (1.08 - 1.27)
Carotid-Upper Arm PTT (ms)	52 (48 - 56)	52 (48 - 56)	52 (48 - 56)
Carotid-Ankle PTT (ms)	136 (124 - 148)	136 (120 - 148)	136 (123 - 148)

5.3.1.1. Training Results

Table 5-2 shows the model parameters associated with all the GTFs and ITFs considered in the training stage. In general, there was large inter-individual variability in all the model parameters. Interestingly, τ_2 exhibited the smallest variability (17.8 % IQR relative to the median value), while η_{12} and η_{22} exhibited the largest variability

(1216% and 291 % IQR relative to the median value), compared with the rest of the parameters.

Table 5-2- Model parameters estimated from training data (median (IQR)).

	TLG GTF (Arm)	TLS GTF (Arm)	TL GTF (Ankle)	f-ITF	p-ITF1	p-ITF2
τ_1	0.068	0.048	-	0.032 (0.025 - 0.038)	0.052 (0.040 - 0.060)	0.047 (0.039 - 0.055)
η_{11}	0.86	20.48	-	14.54 (9.57 - 22.45)	14.58 (9.89 - 29.94)	14.45
η_{21}	0.64	12.61	-	13.88 (9.26 - 20.15)	11.60 (8.77 - 17.94)	13.88
E_1	0.81	1.43	-	0.33 (0.31 - 0.47)	0.33 (0.31 - 0.47)	0.33 (0.31 - 0.47)
E_2	-	0.16	-	1.63 (1.44 - 2.02)	1.63 (1.44 - 2.02)	1.63 (1.44 - 2.02)
η_{VE}	-	0.63	-	0.22 (0.19~0.26)	0.22 (0.19~0.26)	0.22 (0.19~0.26)
τ_2	-	-	0.13	0.12 (0.11 - 0.13)	0.12	0.14 (0.12 - 0.15)
η_{12}	-	-	431.3	19.3 (8.59 - 243.6)	189.9 (96.49 - 309.7)	121.6 (44.73 - 405.5)
η_{22}	-	-	56.05	1.60 (0.78 - 5.53)	23.72 (7.29 - 47.98)	20.98 (3.45 - 64.97)

Table 5-3 shows the performance of the GTFs and ITFs in terms of the errors associated with the estimation of central BP from diametric PVR waveforms. The arm TLS GTF overall largely outperformed its TLG counterpart and the ankle TL GTF (Table 5-3(a)). Both p-ITFs significantly outperformed the f-ITF (Table 5-3(b)), p-ITF$_1$ and p-ITF$_2$ could reduce the waveform RMSE, SBP and PP errors, and SBP and PP error norm significantly by 44.9% and 36.6%, 62.6% and 59.4%, 38.6% and 34.1%, and 50.0% and 46.2%, respectively, relative to the f-ITF. On the other hand, the performance of the two p-ITFs in estimating central SBP and PP were statistically insignificant. These results led us to investigate the arm TLS GTF and two p-ITFs in the testing stage.

Table 5-3- Performance of the GTFs and ITFs in terms of the errors associated with the estimation of central BP from diametric PVR waveforms in training data. Errors are root-mean-squared across all subjects. SBP: systolic blood pressure. PP: pulse pressure. SBP & PP Error Norm: Euclidean norm of SBP and PP errors. *: Significantly different from the arm TLS GTF ($p < 0.05$ with Holms-Bonferroni correction). †: Significantly different from the f-ITF ($p < 0.05$ with Holms-Bonferroni correction).

Training (N=50)	RMSE (mmHg)	SBP Error (mmHg)	PP Error (mmHg)	SBP & PP Error Norm (mmHg)
Arm TLG GTF	4.39^{*}	4.92^{*}	4.35	6.57^{*}
Arm TLS GTF	3.70	3.52	3.84	5.21
Ankle TL GTF	3.96	4.35	4.65	6.37

Training (N=50)	RMSE (mmHg)	SBP Error (mmHg)	PP Error (mmHg)	SBP & PP Error Norm (mmHg)
f-ITF	3.83	5.37	5.02	7.36
p-ITF$_1$	$2.11^{\dagger}$	$2.01^{\dagger}$	$3.08^{\dagger}$	$3.68^{\dagger}$
p-ITF$_2$	$2.43^{\dagger}$	$2.18^{\dagger}$	$3.31^{\dagger}$	$3.96^{\dagger}$

5.3.1.2. Testing Results

Table 5-4 shows the performance of the arm TLS GTF and two p-ITFs in terms of the errors associated with the estimation of central BP from diametric PVR waveforms, and Figure 5-2 shows an illustrative example of central BP waveforms estimated from these transfer functions under low, middle, and high PP amplification. Both p-ITFs significantly outperformed the arm TLS GTF: when root-mean-squared across all 114 testing subjects, p-ITF$_1$ and p-ITF$_2$ could reduce the waveform RMSE, SBP and PP errors, and SBP and PP error norm significantly by 37.8% and 32.8%, 43.4% and 47.2%, 25.6%, and 24.8%, and 32.9% and 34.1%, respectively, relative to the arm TLS GTF.

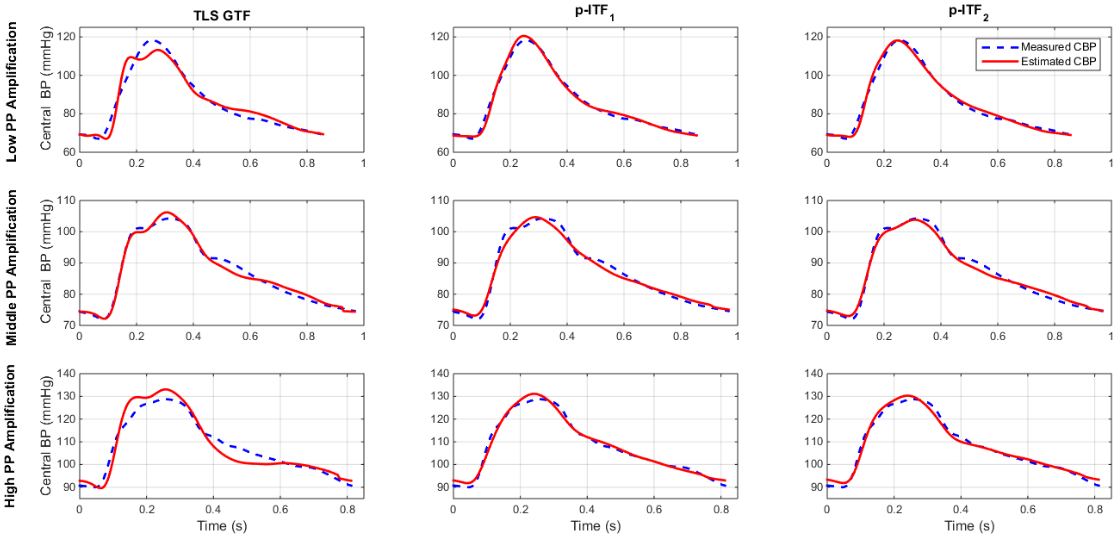

Figure 5-2- An illustrative example of central BP waveforms estimated from the arm TLS GTF, p-ITF1, and p-ITF2 under the low, middle, and high PP amplification.

Table 5-4- Performance of the arm TLS GTF and p-ITFs in terms of the errors associated with the estimation of central BP from diametric PVR waveforms in testing data. Errors are root-mean-squared across all subjects. SBP: systolic blood pressure. PP: pulse pressure. SBP & PP Error Norm: Euclidean norm of SBP and PP errors. *: Significantly different from the arm TLS GTF ($p < 0.05$ with Holms-Bonferroni correction).

Testing (N=114)	RMSE (mmHg)	SBP Error (mmHg)	PP Error (mmHg)	SBP & PP Error Norm (mmHg)
Arm TLS GTF	3.20	3.43	3.79	5.11
p-ITF$_1$	1.99^*	1.94^*	2.82^*	3.43^*
p-ITF$_2$	2.15^*	1.81^*	2.85^*	3.37^*

Figure 5-3 shows the correlation and limits of agreement between the reference (in terms of carotid-ankle) versus estimated aortic SBP, PP, PP amplification (based on the estimated central BP and measured ankle PVR), and PTT (τ_2). Both p-ITFs could estimate aortic SBP (r=1.00), PP (r=0.99), PP amplification (p-ITF$_1$: r-0.90; p-ITF$_2$: r=0.88), and PTT (p-ITF$_2$: r=0.78) that were closely correlated with their respective reference counterparts. The bias and confidence interval were also adequately small: the bias and confidence interval for aortic SBP, PP, PP amplification, and PTT were 0.4% and 3.2% (p-ITF$_1$) and 0.6% and 2.8% (p-ITF$_2$), 4.5% and 9.8% (p-ITF$_1$) and

5.0% and 8.9% (p-ITF$_2$), 5.7% and 12.3% (p-ITF$_1$) and 6.3% and 13.1% (p-ITF$_2$), and 0.8% and 33.4% (p-ITF$_2$), respectively, of the respective median values (Table 5-1). As a comparison, PP amplification based on the central BP estimated from the arm TLS GTF and the measured ankle PVR was significantly less correlated with the reference aortic PP amplification (r=0.66).

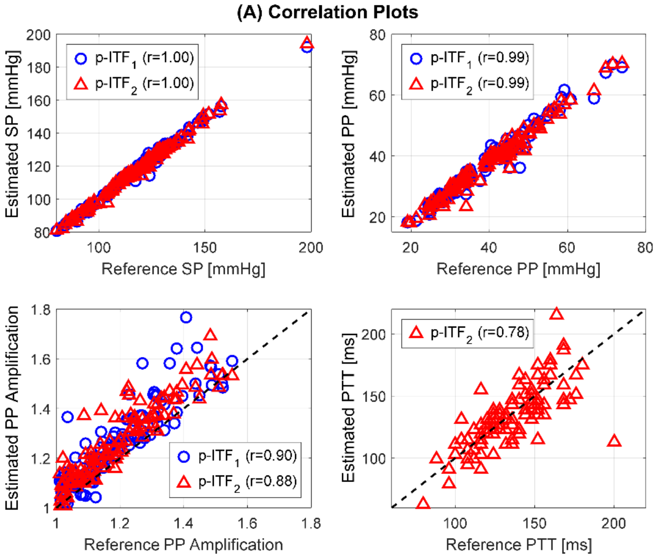
(A) Correlation Plots

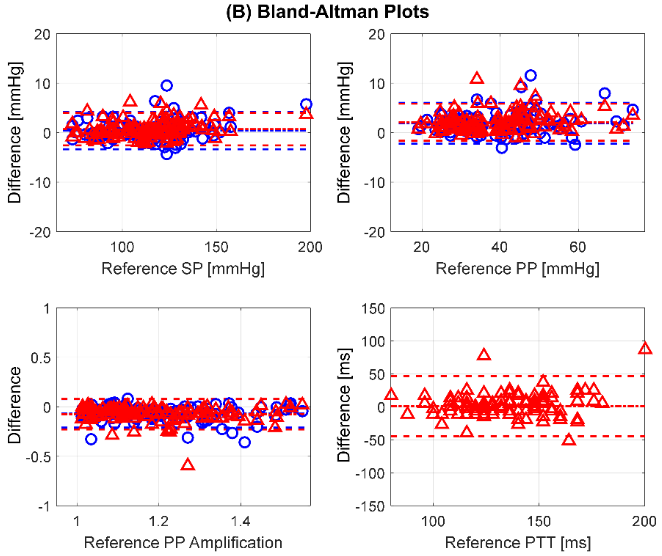
(B) Bland-Altman Plots

Figure 5-3- Correlation (A) and limits of agreement (B) between reference versus estimated aortic SBP, PP, PP amplification, and PTT. Reference aortic SBP, PP, PP amplification, and PTT are based on measured carotid BP and ankle PVR waveforms. Estimated aortic SBP, PP, PP amplification, and PTT are based on central BP estimated by p-ITF and measured ankle PVR.

Table 5-5 shows the performance of the arm TLS GTF and two p-ITFs in subjects associated with low, middle, and high PP amplification. The superiority of the p-ITFs to arm TLS GTF was all in all consistent across all the PP amplification regimes, but especially in low and high PP amplification regimes. When root-mean-squared across all 38 testing subjects with low PP amplification, p-ITF$_{1,}$ and p-ITF$_2$ could reduce the waveform RMSE, SBP and PP errors, and SBP and PP error norm significantly by 38.6% and 35.9%, 39.1% and 46.3%, 22.5% and 26.6%, and 29.5% and 34.8%, respectively, relative to the arm TLS GTF. When root-mean-squared across all 38 testing subjects with high PP amplification, p-ITF$_{1,}$ and p-ITF$_2$ could reduce the waveform RMSE, SBP and PP errors, and SBP and PP error norm significantly by 36.8% and 28.9%, 55.1% and 67.6%, 41.6% and 50.5%, and 46.8% and 56.8%, respectively, relative to the arm TLS GTF.

Table 5-5- Performance of the arm TLS GTF and p-ITFs in subjects associated with low, middle, and high PP amplification. Errors are root-mean-squared across all subjects. SBP: systolic blood pressure. PP: pulse pressure. Norm: Euclidean norm of SBP and PP errors. *: Significantly difference from the arm TLS GTF ($p < 0.05$ with Holms-Bonferroni correction).

Testing (N=114)	Low (1.02 – 1.30)				Middle (1.31 – 1.38)				High (1.38 – 1.58)			
	RMSE	SBP E.	PP E.	Norm	RMSE	SBP E.	PP E.	Norm	RMSE	SBP E.	PP E.	Norm
Arm TLS GTF	3.77	4.67	5.15	6.96	2.94	2.22	2.15	3.09	2.80	2.91	3.46	4.52
p-ITF$_1$	2.32*	2.85*	3.99	4.90*	1.84*	1.24*	1.96	2.32	1.77*	1.30*	2.02*	2.41*
p-ITF$_2$	2.42*	2.51*	3.78	4.54*	2.01*	1.64*	2.65	3.12	1.99*	0.94*	1.71*	1.95*

5.4. Discussion

The proposed p-ITFs (which significantly outperformed the f-ITF in the training stage) displayed significantly superior performance to the arm TLS GTF (which was the best performing GTF obtained in the training stage) in estimating central BP waveform in blind testing (Table 5-4). It has been shown that an f-ITF based on invasive diametric arterial pulse waveforms could estimate central BP waveform more accurately than an arm TL GTF[14], [35]. Additionally in this study, it is found that the f-ITF did not perform as well as the arm TLS GTF when realized with diametric PVR waveforms (Table 5-3), which is presumably attributed to two reasons: (1) PVR waveforms are less informative than arterial pulse (e.g., BP) waveforms with their high-frequency contents lost due to the arterial and tissue viscoelasticity, and (2) non-invasive f-ITF involves more complex arterial line models with increased number of parameters than its invasive counterpart. It is also shown that partial individualization of the arterial line models (i.e., the p-ITFs) could largely enhance the performance of the ITF, perhaps via the regularization of the parameter estimation process for the arterial line models. It is important to emphasize that the p-ITFs considered in this study are built upon solid rationale and insight. First, the p-ITF$_1$ was motivated by the observation from Table 5-2 that τ_2 showed the smallest inter-individual variability among all the arterial line model parameters and may thus be fixed at a nominal value. Second, the p-ITF$_2$ was motivated by the widely accepted knowledge that the arterial line model exhibits much larger sensitivity to its PTT parameter τ_j than the polynomial parameters η_{ij}, $i, j = 1{,}2$[14], [31], [35]. It is worth to note that although viscoelastic parameters have small variability and high variance and uncertainty in identifying, in section 3.5.3, a two-step optimization method is suggested to accurately identify the viscoelastic parameters independently.

According to Table 5-2, the ankle line polynomial parameters (η_{12} and η_{22}) showed larger inter-individual variability than the arm line polynomial parameters (η_{11}

and η_{21}). Further, some pervious work indicates that η_{11} and η_{21} are subject to larger estimation uncertainty than η_{12} and η_{22}[14], [35]. Hence, it made sense to regularize the parameter estimation by fixing η_{11} and η_{21} to appropriate nominal values in considering viable options for p-ITF. Therefore, it was not surprising that p-ITF$_1$ and p-ITF$_2$ examined in this study performed very well. However, it must be noted that the efficacy of p-ITF$_1$ may not generalize to subjects whose PTT drastically deviate from the population-average nominal value (120 ms), whereas p-ITF$_2$ may still generalize well to a wider range of subjects.

The proposed p-ITFs (p-ITF$_2$ in particular) could estimate a number of CV risk predictors solely based on non-invasive diametric pulse measurements (i.e., without requiring any direct measurement of central pulse waveform): aortic SBP, PP, PP amplification, and PTT. These CV risk predictors were estimated from the individually estimated arterial line models (i.e., τ_2 as aortic PTT [77]) and central BP waveform (i.e., peak and pulse amplitude of the estimated central BP waveform as aortic SBP and PP) in conjunction with the measured PVR waveform (i.e., the ratio between the amplitudes of estimated central BP and ankle PVR waveforms as aortic PP amplification). Encouragingly, the CV risk predictors thus estimated were closely correlated with the reference CV risk predictors derived from carotid BP and ankle PVR waveform measurements with tight limits of agreement (Figure 5-3). In prior work Hahn et al. showed that an ITF based on invasive arterial BP waveforms could track the time-varying PTT in a subject [35], [71]. The results obtained from this study suggest that aortic PTT and other CV risk predictors may be monitored conveniently through time. Currently, non-invasive measurement of aortic BP, PP amplification, and

PTT resorts to carotid-femoral tonometry procedure, which requires costly equipment and trained operators to measure both central and distal arterial pulse waveforms. Technologies to incorporate the functionality to estimate central BP from arm PVR waveform into today's arm cuff devices exist [65]–[69]. However, these technologies have limitations in estimating aortic PP amplification and PTT due to the absence of distal aortic pulse measurement. In this regard, obviating the measurement of central pulse waveform in estimating a range of CV risk predictors may be viewed as a significant innovation of this study. That being said, it must also be emphasized that arm cuff device equipped with a GTF may still be a convenient option for brachial and central BP measurement; if CV risk predictors requiring the measurement of the distal aortic pulse is not of primary interest.

Analysing the performance of the arm TLS GTF and p-ITFs obtained from the blind testing with respect to the degree of PP amplification, the p-ITFs were superior to the arm TLS GTF independently of PP amplification. In particular, the p-ITFs were significantly superior to the arm TLS GTF in all error metrics in subjects with low and high PP amplification regimes (except the PP error in low PP amplification regime). The difference between the p-ITFs and the arm TLS GTF was less significant in the middle PP amplification regime, which may be attributed to the fact that the arm TLS GTF was trained to perform adequately in all the PP amplification regimes, and thus, it is expected to perform relatively better in subjects with middle than low and high PP amplification.

As a last remark, it must be emphasized that the arm TLS GTF is a secondary contribution of this study regardless of the focus of this study on the ITF. Lee et al.

showed in their work based on this data set that, on an individualized basis, arm TLS model outperformed its TLG counterpart and individualized ankle TL model in estimating central BP waveform from the respective distal PVR waveforms [78]. The results obtained in this study (Table 3(a)) show that our previous findings persist even on a generalized basis. Noting that (at least a subset of) prior work on the GTF resorted to the assumption that arm PVR waveform may be used as a surrogate of brachial BP waveform [63], the arm TLS GTF may offer opportunities to improve the efficacy of GTF in estimating central BP waveform.

5.4.1. Study Limitation

This study has a few limitations. First, we examined only two options for the p-ITF. On one hand, the two p-ITFs were built upon solid rationale and insight, and for that reason, were shown to perform very well. On the other hand, there are many alternatives to constructing p-ITF that could have been explored. In this regard, more extensive investigation of the p-ITF approach may be a rewarding exercise. Second, we examined only the use of a pair of PVR waveforms from the arm and ankle for the realization of the proposed approach. Other distal sites such as ear, finger, and toe may afford viable options for practical implementation of the approach. In addition, the efficacy of the approach may benefit from increasing the number of measurements, e.g., by leveraging richer information contents to enhance ITFs' robustness. Future work must explore such opportunities. Third, the ethnic group we examined was rather homogeneous (Asians). Future work must examine the performance of the proposed approach in diverse ethnic groups in order to truly establish its efficacy.

5.5. Conclusion

A novel multiple measurement information fusion approach to non-invasive estimation of CV risk predictors from PVR waveforms measured at diametric locations in the body is proposed and validated. This approach has a few advantages compared with the state-of-the-art techniques for CV risk predictors estimation. First, it may be more accurate than the traditional GTF approach by virtue of subject specificity. Second, it may offer a more comprehensive assessment of CV risk in a subject by virtue of its ability to estimate a number of CV risk predictors. Third, it may enable convenient CV risk predictor monitoring by obviating the measurement of central pulse waveform (which usually requires costly procedures and trained operators).

Chapter 6: Conclusions

Cardiovascular diseases are the main cause of death in the US and around the world these days. Due to the increasing costs and the population size being affected, early detection and timely treatment of CVD are crucial. Many studies have shown that central BP waveform is a good CV risk indicator. However, because of the difficulty in measuring it, this waveform is not widely used in clinical practice. In this thesis, we proposed a new model-based system identification procedure to accurately estimate the central BP waveform by means of two non-invasive peripheral signals. Then, the estimated Central BP waveform was used to extract the CV risk predictors. A new de-convolution technique is also developed to compensate for the modeling error. The advantages of this method over the existing techniques are that this approach is based on non-invasive peripheral signals (which are easy to measure with low-cost sensors) and, more importantly, assessment is personalized.

6.1. Summary

In summary, the main contributions of this thesis are as follow:

- First, we developed a mathematical model that relates invasive CV circulatory signals to non-invasively measured pressure and volume signals (Chapter 3).
- Second, we proposed a systematical method to solve the system identification problem in order to estimate a personalized arterial tree model and aortic BP signal for a multi-channel class of systems with non-invasive circulatory signals (Chapter 3).

- Third, we formulated a mathematical model for estimating central BP by means of low-cost and already widely used, PVR cuffs (Chapter 3).
- Fourth, This model is validated using experimental data from PVR measurements of 10 human subjects (Chapter 3).
- Fifth, a closed-loop based de-convolution algorithm for coprime multi-channel systems is formulated to estimate the aortic BP waveform based on state estimation techniques (Chapter 4).
- Sixth, the feasibility of the proposed de-convolution algorithm is examined using experimental data (Chapter 4).
- Seventh, we presented a multiple measurement information fusion approach to estimate the CV risk predictors non-invasively from PVR waveforms (Chapter 5).
- Eighth, the validity of this approach is studied using a large dataset of 164 blood pressure measurements from human subjects (Chapter 5).
- Ninth, we compared the results of the proposed method with the results obtained from the GTF technique (Chapter 5).

6.2. Future work

The proposed future work direction includes:

First: the extension of the proposed input de-convolution algorithm to incorporate advanced state estimation techniques with rigorous robustness guarantee against errors and uncertainties associated with the channel dynamics, as well as intensive evaluation of the algorithm in a larger dataset as well as other real-world applications.

Second, we used non-invasive PVR waveforms because it is widely used in today’s clinical practice. However, as the technology is advancing, variety of new wearable sensors are emerging in CV health monitoring. Expanding this work to use these kind of sensors will definitely have great advantage in advancing this field.

Third, the proposed model-based cardiovascular risk predictor technique should be extended to investigate the CVDs prediction approaches. The relation between the parameters of the model and estimated CV risk predictors, and CV events should be investigated more rigorously.

And finally, at the next level, this CVD prediction system should be implemented in clinical practice for CV health monitoring as CVDs diagnostic system using low-cost and non-invasive measurements in different groups of subjects and compare this approach with traditional techniques that are now widely used. As this is the ultimate goal of this work to equip doctors and physicians with more accurate tools to overcome CVDs and identify them at the early stages using low-cost measurements.

Bibliography

[1] E. J. Benjamin *et al.*, *Heart Disease and Stroke Statistics'2019 Update: A Report from the American Heart Association*, vol. 135, no. 10. 2017.

[2] M. E. Safar *et al.*, "Central pulse pressure and mortality in end-stage renal disease.," *Hypertens. (Dallas, Tex. 1979)*, vol. 39, no. 3, pp. 735–8, Mar. 2002.

[3] C. M. McEniery, J. R. Cockcroft, M. J. Roman, S. S. Franklin, and I. B. Wilkinson, "Central blood pressure: current evidence and clinical importance," *Eur. Heart J.*, vol. 35, no. 26, pp. 1719–1725, Jul. 2014.

[4] A. Qasem and A. Avolio, "Determination of aortic pulse wave velocity from waveform decomposition of the central aortic pressure pulse.," *Hypertens. (Dallas, Tex. 1979)*, vol. 51, no. 2, pp. 188–95, Feb. 2008.

[5] M. J. Roman *et al.*, "Central Pressure More Strongly Relates to Vascular Disease and Outcome Than Does Brachial Pressure: the Strong Heart Study," *Hypertension*, vol. 50, no. 1, pp. 197–203, Jul. 2007.

[6] M. J. Roman, P. M. Okin, J. R. Kizer, E. T. Lee, B. V Howard, and R. B. Devereux, "Relations of Central and Brachial Blood Pressure to Left Ventricular Hypertrophy and Geometry: the Strong Heart Study," *J. Hypertens.*, vol. 28, no. 2, pp. 384–8, Feb. 2010.

[7] J. M. Ferguson, J. Minas, S. Siapantas, P. A. Komesaroff, and K. Sudhir, "Effects of a Fixed-Dose ACE Inhibitor-diuretic Combination on Ambulatory Blood Pressure and Arterial Properties in Isolated Systolic Hypertension," *J. Cardiovasc. Pharmacol.*, vol. 51, no. 6, pp. 590–5, Jun. 2008.

[8] A. Mahmud and J. Feely, "Beta-Blockers Reduce Aortic Stiffness in

Hypertension but Nebivolol, Not Atenolol, Reduces Wave Reflection," *Am. J. Hypertens.*, vol. 21, no. 6, pp. 663–7, Jun. 2008.

[9] B. Williams *et al.*, "Differential Impact of Blood Pressure-lowering Drugs on Central Aortic Pressure and Clinical Outcomes: Principal Results of the Conduit Artery Function Evaluation (CAFE) Study," *Circulation*, vol. 113, no. 9, pp. 1213–25, Mar. 2006.

[10] M. Goyal, N. Priyadarsini, S. C. Singh, and S. C. Mahapatra, "Clinical Importance in Hypertensive Disorders during Preg-nancy," *Hypertens J*, vol. 3, no. 4, pp. 173–177.

[11] C. H. Chen *et al.*, "Estimation of Central Aortic Pressure Waveform by Mathematical Transformation of Radial Tonometry Pressure. Validation of Generalized Transfer Function," *Circulation*, vol. 95, no. 7, pp. 1827–36, Apr. 1997.

[12] J. E. Sharman *et al.*, "Validation of a generalized transfer function to noninvasively derive central blood pressure during exercise.," *Hypertens. (Dallas, Tex. 1979)*, vol. 47, no. 6, pp. 1203–8, Jun. 2006.

[13] B. Fetics, E. Nevo, C. H. Chen, and D. A. Kass, "Parametric Model Derivation of Transfer Function for Noninvasive Estimation of Aortic Pressure by Radial Tonometry," *IEEE Trans. Biomed. Eng.*, vol. 46, no. 6, pp. 698–706, Jun. 1999.

[14] N. Fazeli *et al.*, "Subject-Specific Estimation of Central Aortic Blood Pressure via System Identification: Preliminary In-human Experimental Study," *Med. Biol. Eng. Comput.*, vol. 52, no. 10, pp. 895–904, Oct. 2014.

[15] F.-H. Ding, W.-X. Fan, R.-Y. Zhang, Q. Zhang, Y. Li, and J.-G. Wang,

"Validation of the Noninvasive Assessment of Central Blood Pressure by the SphygmoCor and Omron Devices Against the Invasive Catheter Measurement," *Am. J. Hypertens.*, vol. 24, no. 12, pp. 1306–1311, 2011.

[16] D. Gallagher, A. Adji, and M. F. O'Rourke, "Validation of the Transfer Function Technique for Generating Central from Peripheral Upper Limb Pressure Waveform," *Am. J. Hypertens.*, vol. 17, no. 11 Pt 1, pp. 1059–67, Nov. 2004.

[17] C. H. Chen *et al.*, "Validation of carotid artery tonometry as a means of estimating augmentation index of ascending aortic pressure.," *Hypertension*, vol. 27, no. 2, pp. 168–75, Feb. 1996.

[18] R. Mukkamala *et al.*, "Toward Ubiquitous Blood Pressure Monitoring via Pulse Transit Time: Theory and Practice," *IEEE Trans. Biomed. Eng.*, vol. 62, no. 8, pp. 1879–1901, 2015.

[19] K. Hirata, M. Kawakami, and M. F. O'Rourke, "Pulse wave analysis and pulse wave velocity: a review of blood pressure interpretation 100 years after Korotkov.," *Circ. J.*, vol. 70, no. 10, pp. 1231–1239, 2006.

[20] P. Salvi *et al.*, "Comparative study of methodologies for pulse wave velocity estimation," *J. Hum. Hypertens.*, vol. 22, no. 10, pp. 669–677, 2008.

[21] S. Laurent *et al.*, "Expert consensus document on arterial stiffness: Methodological issues and clinical applications," *Eur. Heart J.*, vol. 27, no. 21, pp. 2588–2605, 2006.

[22] E. Agabiti-Rosei *et al.*, "Central blood pressure measurements and antihypertensive therapy: A consensus document," *Hypertension*, vol. 50, no. 1, pp. 154–160, 2007.

[23] G. F. Mitchell *et al.*, “Changes in Arterial Stiffness and Wave Reflection With Advancing Age in Healthy Men and Women The Framingham Heart Study,” 2004.

[24] W. Nichols, M. F. O’Rourke, and C. Vlachopoulos, Eds., *McDonald’s Blood Flow in Arteries: Theoretical, Experimental and Clinical Principles*, 6th ed. CRC Press, 2011.

[25] J. Liu, H.-M. Cheng, C.-H. Chen, S.-H. Sung, J.-O. Hahn, and R. Mukkamala, “Patient-Specific Oscillometric Blood Pressure Measurement: Validation for Accuracy and Repeatability,” *IEEE J. Transl. Eng. Heal. Med.*, vol. 5, pp. 1–10, 2017.

[26] Y.-T. Shih, H.-M. Cheng, S.-H. Sung, W.-C. Hu, and C.-H. Chen, “Comparison of two generalized transfer functions for measuring central systolic blood pressure by an oscillometric blood pressure monitor,” *J. Hum. Hypertens.*, vol. 27, no. 3, pp. 204–210, Mar. 2013.

[27] P. K. Lim *et al.*, “Improved measurement of blood pressure by extraction of characteristic features from the cuff oscillometric waveform,” *Sensors (Switzerland)*, vol. 15, no. 6, pp. 14142–14161, 2015.

[28] M. Karamanoglu, M. F. O’Rourke, A. P. Avolio, and R. P. Kelly, “An Analysis of the Relationship Between Central Aortic and Peripheral Upper Limb Pressure Waves in Man,” *Eur. Heart J.*, vol. 14, no. 2, pp. 160–7, Feb. 1993.

[29] S. Soderstrom, S. Söderström, G. Nyberg, M. F. O’Rourke, J. Sellgren, and J. Pontén, “Can a Clinically Useful Aortic Pressure Wave Be Derived from a Radial Pressure Wave?,” *Br. J. Anaesth.*, vol. 88, no. 4, pp. 481–8, Apr. 2002.

[30] S. A. Hope, I. T. Meredith, and J. D. Cameron, “Arterial Transfer Functions and the Reconstruction of Central Aortic Waveforms: Myths, Controversies and Misconceptions,” *J. Hypertens.*, vol. 26, no. 1, pp. 4–7, Jan. 2008.

[31] M. Sugimachi, T. Shishido, K. Miyatake, and K. Sunagawa, “A New Model-Based Method of Reconstructing Central Aortic Pressure from Peripheral Arterial Pressure,” *Jpn. J. Physiol.*, vol. 51, no. 2, pp. 217–22, 2001.

[32] W. J. Stok, B. E. Westerhof, and J. M. Karemaker, “Changes in Finger-Aorta Pressure Transfer Function During and After Exercise,” *J. Appl. Physiol.*, vol. 101, no. 4, pp. 1207–14, Oct. 2006.

[33] W. J. Stok, B. E. Westerhof, I. Guelen, and J. M. Karemaker, “Aortic Pressure Wave Reconstruction During Exercise Is Improved by Adaptive Filtering: a Pilot Study,” *Med. Biol. Eng. Comput.*, vol. 49, no. 8, pp. 909–16, Aug. 2011.

[34] D. B. D. B. McCombie, A. T. A. T. Reisner, and H. H. H. H. Asada, “Laguerre-Model Blind System Identification: Cardiovascular Dynamics Estimated from Multiple Peripheral Circulatory Signals,” *IEEE Trans. Biomed. Eng.*, vol. 52, no. 11, pp. 1889–901, Nov. 2005.

[35] J.-O. Hahn, A. T. Reisner, and H. H. Asada, “Blind Identification of Two-Channel IIR Systems with Application to Central Cardiovascular Monitoring,” *J. Dyn. Syst. Meas. Control*, vol. 131, no. 5, p. 051009, Sep. 2009.

[36] J.-O. Hahn, A. T. Reisner, and H. Harry Asada, “Modeling and 2-Sensor Blind Identification of Human Cardiovascular System,” *Control Eng. Pract.*, vol. 17, no. 11, pp. 1318–1328, Nov. 2009.

[37] G. Swamy, Q. Ling, T. Li, and R. Mukkamala, “Blind Identification of the Aortic

Pressure Waveform from Multiple Peripheral Artery Pressure Waveforms," *Am. J. Physiol. Heart Circ. Physiol.*, vol. 292, no. 5, pp. H2257-64, May 2007.

[38] A. S. Abutaleb, M. E.-S. Waheed, and N. M. Elhamy, "Multichannel Blind Deconvolution Using the Stochastic Calculus for the Estimation of the Central Arterial Pressure," *Math. Probl. Eng.*, vol. 2010, pp. 1–22, 2010.

[39] A. S. Abutaleb, M. El-Sayed Waheed, and N. M. Elhamy, "Blind Deconvolution of the Aortic Pressure Waveform Using the Malliavin Calculus," *Math. Probl. Eng.*, vol. 2010, p. 27, 2010.

[40] Y. Zhang and H. H. Asada, "Blind System Identification of Noncoprime Multichannel Systems and its Application to Noninvasive Cardiovascular Monitoring," *J. Dyn. Syst. Meas. Control*, vol. 126, no. 4, pp. 834–847, Dec. 2004.

[41] G. Zhang, J.-O. Hahn, and R. Mukkamala, "Tube-Load Model Parameter Estimation for Monitoring Arterial Hemodynamics," *Front. Physiol.*, vol. 2, p. 72, Jan. 2011.

[42] M. N. Nihat Özkaya, "Mechanical Properties of Biological Tissues," in *Fundamentals of biomechanics : equilibrium, motion, and deformation*, 2nd ed., New York: Springer, 1999.

[43] S. Choi and A. Cichocki, "Cascade Neural Networks for Multichannel Blind Deconvolution," *Appear. Electron. Lett.*, vol. 34, no. 1, pp. 1186–1187, 1998.

[44] F. Sroubek and J. Flusser, "Multichannel Blind Deconvolution of Spatially Misaligned Images," *IEEE Trans. IMAGE Process.*, vol. 14, no. 7, 2005.

[45] Z. Ghasemi, C. Kim, E. Ginsberg, A. Gupta, and J.-O. Hahn, "Model-Based

Blind System Identification Approach to Estimation of Central Aortic Blood Pressure Waveform From Noninvasive Diametric Circulatory Signals," *J. Dyn. Syst. Meas. Control*, vol. 139, no. June, pp. 1–10, 2017.

[46] A. S. Abutaleb, M. E.-S. Waheed, and N. M. Elhamy, "Multichannel Blind Deconvolution Using the Stochastic Calculus for the Estimation of the Central Arterial Pressure," *Math. Probl. Eng.*, vol. 2010, pp. 1–21, 2010.

[47] J. O. Hahn, D. B. McCombie, A. T. Reisner, H. M. Hojman, and A. Harry, "Identification of multichannel cardiovascular dynamics using dual laguerre basis functions for noninvasive cardiovascular monitoring," *IEEE Trans. Control Syst. Technol.*, vol. 18, no. 1, pp. 170–176, 2010.

[48] G. Zhang, J. O. Hahn, and R. Mukkamala, "Tube-load model parameter estimation for monitoring arterial hemodynamics," *Front. Physiol.*, vol. 2 NOV, no. November, pp. 1–18, 2011.

[49] Y. Hua, "Blind Methods of System Identification," *Circuits, Syst. Signal Process.*, vol. 21, no. 1, pp. 91–108, 2002.

[50] F. Alberge, P. Duhamel, and M. Nikolova, "Adaptive Solution for Blind Identification / Equalization Using Deterministic Maximum Likelihood," *IEEE Trans. Signal Process.*, vol. 50, no. 4, pp. 923–936, 2002.

[51] M. L. Gürelli and C. L. Nikias, "EVAM: An Eigenvector-Based Deconvolution of Input Colored Signals," *IEEE Tran. Signal Process.*, vol. 43, no. 1, pp. 134–149, 1995.

[52] G. Drzewiecki, V. Bansal, E. Karam, R. Hood, and H. Apple, "Mechanics of the Occlusive Arm Cuff and Its Application as a Volume Sensor," *IEEE Trans.*

Biomed. Eng., vol. 40, no. 7, pp. 704–8, Jul. 1993.

[53] W.-C. Yu, S.-Y. Chuang, Y.-P. Lin, and C.-H. Chen, "Brachial-Ankle vs Carotid-Femoral Pulse Wave Velocity as a Determinant of Cardiovascular Structure and Function," *J. Hum. Hypertens.*, vol. 22, no. 1, pp. 24–31, Jan. 2008.

[54] M. Rashedi *et al.*, "Comparative Study on Tube-Load Modeling of Arterial Hemodynamics in Humans.," *J. Biomech. Eng.*, vol. 135, no. 3, p. 31005, Mar. 2013.

[55] M. Abdollahzade, C.-S. Kim, N. Fazeli, B. A. Finegan, M. Sean McMurtry, and J.-O. Hahn, "Data-Driven Lossy Tube-Load Modeling of Arterial Tree: In-Human Study.," *J. Biomech. Eng.*, vol. 136, no. 10, p. 101011, Oct. 2014.

[56] G. Drzewiecki, R. Hood, and H. Apple, "Theory of the Oscillometric Maximum and the Systolic and Diastolic Detection Ratios," *Ann. Biomed. Eng.*, vol. 22, no. 1, pp. 88–96, Jan. 1994.

[57] J. M. ASKEY, "The Auscultatory Gap in Sphygmomanometry," *Ann. Intern. Med.*, vol. 80, no. 1, p. 94, Jan. 1974.

[58] M. Green, D. A. Paulus, V. P. Roan, and J. van der Aa, "Comparison between oscillometric and invasive blood pressure monitoring during cardiac surgery," *Int. J. Clin. Monit. Comput.*, vol. 1, no. 1, pp. 21–26, Mar. 1984.

[59] A. Bur *et al.*, "Accuracy of oscillometric blood pressure measurement according to the relation between cuff size and upper-arm circumference in critically ill patients.," *Crit. Care Med.*, vol. 28, no. 2, pp. 371–6, Feb. 2000.

[60] S. Ribezzo, E. Spina, S. Di Bartolomeo, and G. Sanson, "Noninvasive

techniques for blood pressure measurement are not a reliable alternative to direct measurement: a randomized crossover trial in ICU.," *ScientificWorldJournal.*, vol. 2014, p. 353628, Jan. 2014.

[61] Q. Shangguan *et al.*, "The impact of arm circumference on noninvasive oscillometric blood pressure referenced with intra-aortic blood pressure.," *Blood Press. Monit.*, vol. 20, no. 6, pp. 316–9, Dec. 2015.

[62] M. R. Nelson, J. Stepanek, M. Cevette, M. Covalciuc, R. T. Hurst, and A. J. Tajik, "Noninvasive Measurement of Central Vascular Pressures with Arterial Tonometry: Clinical Revival of the Pulse Pressure Waveform?," *Mayo Clin. Proc.*, vol. 85, no. 5, pp. 460–72, May 2010.

[63] Y.-T. Shih, H.-M. Cheng, S.-H. Sung, W.-C. Hu, and C.-H. Chen, "Comparison of two generalized transfer functions for measuring central systolic blood pressure by an oscillometric blood pressure monitor.," *J. Hum. Hypertens.*, vol. 27, no. 3, pp. 204–10, 2013.

[64] H. Cheng, S. Sung, Y. Shih, S. Chuang, W. Yu, and C. Chen, "Measurement Accuracy of a Stand-Alone Oscillometric Central Blood Pressure Monitor : A Validation Report for Microlife WatchBP Office Central," vol. 26, no. January, 2013.

[65] H. Cheng *et al.*, "Estimation of central systolic blood pressure using an oscillometric blood pressure monitor," *Hypertens. Res.*, vol. 33, no. 6, pp. 592–599, 2010.

[66] H. Cheng, S. Sung, Y. Shih, S. Chuang, W. Yu, and C. Chen, "Measurement of Central Aortic Pulse Pressure : Noninvasive Brachial Cuff-Based Estimation by

a Transfer Function Vs . a Novel Pulse Wave Analysis Method," *Am. J. Hypertens.*, vol. 25, no. 11, pp. 1162–1169, 2012.

[67] W. J. Verberk, H.-M. Cheng, L.-C. Huang, C.-M. Lin, Y.-P. Teng, and C.-H. Chen, "Practical Suitability of a Stand-Alone Oscillometric Central Blood Pressure Monitor: A Review of the Microlife WatchBP Office Central.," *Pulse (Basel, Switzerland)*, vol. 3, no. 3–4, pp. 205–16, 2016.

[68] T. G. Papaioannou *et al.*, "Accuracy of commercial devices and methods for noninvasive estimation of aortic systolic blood pressure: a systematic review and meta-analysis of invasive validation studies," *J. Hypertens.*, vol. 34, no. 7, pp. 1237–1248, 2016.

[69] G. Pucci *et al.*, "Evaluation of the Vicorder, a novel cuff-based device for the noninvasive estimation of central blood pressure," *J. Hypertens.*, vol. 31, no. 1, pp. 77–85, 2013.

[70] J. G. Kips *et al.*, "Comparison of central pressure estimates obtained from SphygmoCor, Omron HEM-9000AI and carotid applanation tonometry," *J. Hypertens.*, vol. 29, no. 6, pp. 1115–1120, 2011.

[71] J.-O. Hahn, A. T. Reisner, and H. H. Asada, "Estimation of pulse transit time using two diametric blood pressure waveform measurements.," *Med. Eng. Phys.*, vol. 32, no. 7, pp. 753–759, 2010.

[72] C. S. Kim, N. Fazeli, M. S. McMurtry, B. a Finegan, and J. O. Hahn, "Quantification of Wave Reflection Using Peripheral Blood Pressure Waveforms," *IEEE J. Biomed. Heal. Informatics*, vol. 19, no. 1, pp. 309–316, 2014.

[73] M. Sinski, G. Styczynski, and C. Szmigielski, “Automated oscillometric measurement of the ankle–brachial index in patients with coronary artery disease,” *Hypertens. Res.*, vol. 36, no. 1, pp. 25–28, 2013.

[74] J. A. Beckman, C. O. Higgins, M. Gerhard-herman, J. A. Beckman, C. O. Higgins, and M. Gerhard-herman, “Automated Oscillometric Determination of the Ankle – Brachial Index Provides Accuracy Necessary for Office Practice,” 2006.

[75] F. Saladini, E. Benetti, S. Masiero, and P. Palatini, “Accuracy of Microlife WatchBP Office ABI monitor assessed according to the 2002 European Society of Hypertension protocol and the British Hypertension Society protocol,” *Blood Press. Monit.*, vol. 16, no. 5, pp. 258–61, 2011.

[76] R. Kelly and D. Fitchett, “Noninvasive determination of aortic input impedance and external left ventricular power output: A validation and repeatability study of a new technique,” *J. Am. Coll. Cardiol.*, vol. 20, no. 4, pp. 952–963, Oct. 1992.

[77] D. Campo *et al.*, “Measurement of Aortic Pulse Wave Velocity With a Connected Bathroom Scale,” *Am. J. Hypertens.*, pp. 1–8, 2017.

[78] J. Lee *et al.*, “Investigation of Viscoelasticity in the Relationship Between Carotid Artery Blood Pressure and Distal Pulse Volume Waveforms,” *IEEE J. Biomed. Heal. Informatics*, 2017.

[79] K. Abed-Meraim, W. Qiu, and Y. Hua, “Blind System Identification,” *Proc. IEEE*, vol. 85, no. 8, pp. 1310–1322, 1997.

[80] C. T. Chen, *Linear System Theory and Design*, 3rd ed. New York: Oxford

University Press, 1998.

[81] G. F. Franklin, J. D. Powell, and A. Emami-Naeini, *Feedback Control of Dynamic Systems*, 6th ed. Upper Saddle River: Pearson Higher Education, Inc., 1994.